Biomaterials 327 (2026) 123790

Contents lists available at ScienceDirect

Biomaterials

journal homepage: www.elsevier.com/locate/biomaterials

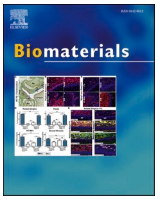

Antioxidase-mimetic artificial biotubes for anti-inflammatory healing and regeneration of vascular injury

Guliyaer Aini [a], Jianmei Ren [b], Haojie Xu [a], Yang Gao [b], Tiantian Li [a], Lang Ma [b], Li Qiu [b], Evgeniya Sheremet [c], Shuang Li [a], Chong Cheng [a], Tian Ma [a,*], Changsheng Zhao [a]

[a] *College of Polymer Science and Engineering, National Key Laboratory of Advanced Polymer Materials, Sichuan University, Chengdu, 610065, China*
[b] *Department of Ultrasound, Frontiers Science Center for Disease-related Molecular Network, National Clinical Research Center for Geriatrics, Med-X Center for Materials, West China Hospital, Sichuan University, Chengdu, 610041, China*
[c] *Tomsk Polytechnic University, Lenina Ave. 30, Tomsk, 634050, Russia*

ARTICLE INFO

Keywords:
Antioxidase-mimic
Artificial grafts
Anti-Inflammation
Angiogenesis promotion
Vascular injury

ABSTRACT

Inflammation is a major obstacle to endothelialization, which is essential to the long-term functionality of cardiovascular implants. Developing efficient antioxidant and inflammation-modulating biotubes for endothelial repair with minimal postsurgical complications represents a compelling clinical challenge. Here, we present the design of an antioxidase-mimic modified artificial biotube (RNP) by integrating Ru cluster-anchored Ni-based metal-organic framework onto a polycaprolactone fiber scaffold. This biotube acts as a biocatalytic reactive oxygen species (ROS) scavenger, modulating the postsurgical microenvironment to suppress the inflammatory cascades and prevent postoperative adhesions efficiently. Our studies reveal that the Ni–O–Ru interface regulates the electronic structure of the Ru active site with rapid charge transfer and enhances the ROS elimination capacity of RNP. These features enable the engineered biotube to mitigate ROS-induced endothelial cell death, promote a regenerative microenvironment, and stimulate vascular regeneration. Consequently, this leads to a robust reparative effect on rat injured arteries. These findings highlight the biocatalytic properties of RNP, offering a promising strategy for developing ROS-scavenging and anti-inflammatory biotubes for vascular repair and the treatment of various oxidative stress-related diseases.

1. Introduction

With the rapid development of interventional cardiology, implantable devices have become important in treating cardiovascular diseases (CVDs) [1,2]. However, the use of non-degradable synthetic vascular prostheses or bare-metal stents during interventional procedures inevitably causes endothelial damage, triggering an upsurge of reactive oxygen species (ROS) release in the inflammatory cascade of the host [3–6]. This leads to delayed endothelialization, intimal hyperplasia, calcification, degradation, and ultimately, failure of cardiovascular implants [7]. Targeted ROS elimination at the injury site has been demonstrated to effectively protect neovascularization and suppress inflammation, critical aspects for the restoration from vascular injury [8–11]. Therefore, the development of ROS-scavenging, inflammation-modulating, and *in vivo* degradable vascular grafts is clinically essential.

Recently, various polymer scaffolds and wound dressings have been developed for application in endothelial repair [12–17]. However, these advanced materials are predominantly used in limited areas such as superficial wound healing and bone defect repairs [18–26], and the elaborate design of cardiovascular grafts remains to be explored. Concurrently, polycaprolactone (PCL), with remarkable biocompatibility, natural degradability, high cost-effectiveness, stability during processing and storage, and outstanding mechanical properties [27–31], has been utilized in the sophisticated design of diverse artificial vascular grafts [27,32–34]. However, existing strategies have not fully addressed critical challenges such as the integration of inflammation alleviation and endothelial repair, therapeutic microenvironment adaptability, and regeneration efficiency. Furthermore, small-diameter vascular grafts (≤6 mm inner diameter) are not yet approved by regulatory agencies. To address these issues, it is imperative to design versatile composite biotubes that adapt to complicated redox dynamics in both ROS scavenging and endothelial regeneration microenvironments.

In biological systems, endogenous antioxidases, such as superoxide

---

* Corresponding author.
E-mail address: matian1991@scu.edu.cn (T. Ma).

https://doi.org/10.1016/j.biomaterials.2025.123790
Received 17 June 2025; Received in revised form 8 September 2025; Accepted 13 October 2025

dismutase (SOD) and catalase (CAT), serve as essential biocatalysts that preserve cellular redox balance by neutralizing ROS and converting them into harmless byproducts. Despite their intrinsic benefits, these natural antioxidants still have several limitations, such as high antigenicity, instability, and delivery challenges, which hinder their clinical application in treating oxidative stress-related vascular diseases [35–37]. Consequently, researchers focused on developing novel biocatalytic ROS-scavenging materials to mimic natural antioxidases for antioxidant therapy [38–45]. Accumulating evidence indicates that SOD–CAT cascade nanozyme systems hold therapeutic promise for inflammatory cardiovascular disorders such as atherosclerosis and myocardial ischemia, as SOD catalyzes the dismutation of $\cdot O_2^-$ into H_2O_2 and O_2, followed by CAT-mediated decomposition of H_2O_2 into H_2O and O_2, thereby constituting a concerted ROS-elimination cascade [46–49]. Inspired by the structure and function of natural enzymes, considerable attention has been attracted to metal-coordination structures, particularly metal-organic frameworks (MOFs), for ROS scavenging and cell protection [50–53]. For instance, a porous nickel-based MOF, mimicking the active sites of the natural Ni-superoxide dismutase (NiSOD), which not only exhibits remarkable SOD-like activity but also is capable of fully activating the interaction between catalytic centers and substrates, thereby promoting multiple injury healing [52,54,55]. Moreover, ruthenium, an element in the iron group, is increasingly used in designing antioxidant nanozymes due to its favorable catalytic properties, high redox stability, and efficient bonding with substrates [56,57]. Ruthenium-based antioxidases, such as Ru-MOFs or Ru composites, have shown promise in treating inflammatory diseases through ROS scavenging [35,58,59]. Particularly, the Ru nanocluster-based antioxidases have demonstrated higher ROS-scavenging efficiency and cell protection compared to isolated Ru sites [56]. However, the ROS-scavenging capacity of monometallic catalysts remains limited, necessitating the development of multi-metal synergistic catalysts for broader ROS spectrum targeting, especially in the high ROS conditions of cardiovascular implants.

Here, to overcome the enormous challenges, we propose the design of antioxidase-mimetic biotubes with Ni/Ru bimetallic catalytic sites through integrating Ru nanocluster-anchored Ni-MOF (RN) onto a PCL fiber scaffold (RNP) for enhanced ROS-scavenging and endothelial

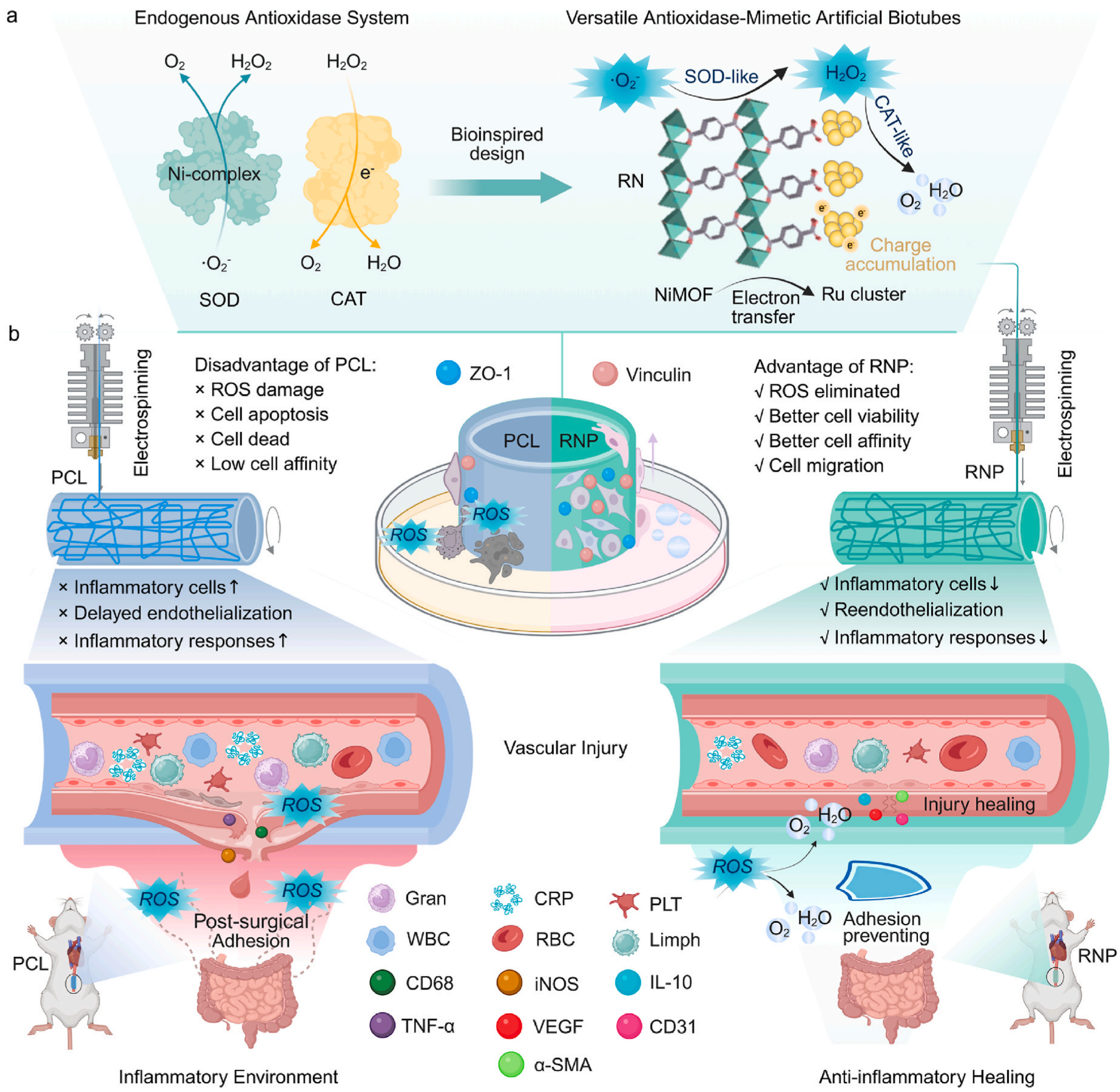

Scheme 1. Schematic process of utilizing RNP biotube to suppress the inflammatory cascades and modulate postsurgical microenvironments in injured arteries. (**a**) The construction of the Ni–O–Ru interface on RN to regulate the electronic structure of active sites and enhance ROS-eliminating capacity. (**b**) The RNP biotube can reduce the number of dead HUVECs by attenuating ROS-induced cell damage, creating powerful reparative microenvironments for injured arteries by inhibiting inflammatory responses, preventing postsurgical adhesion, and promoting the activation of vascular regeneration.

regeneration. This biotube can serve as a biocatalytic ROS scavenger, modulating the postsurgical microenvironment to suppress inflammatory cascades and prevent postoperative adhesions (Scheme 1). This study is motivated by two key aspects: (1) the Ni–O–Ru interface on the Ni-MOF modulates the electronic structure of the Ru active site with rapid charge transfer and increases ROS scavenging capacity; (2) the RNP biotube with broad-spectrum antioxidative properties can effectively counteract oxidative stress and promote endothelial regeneration in the inflammatory microenvironment of postsurgical arteries. As a result, the RNP biotube exhibits remarkable biocatalytic ROS scavenging activities with a high elimination rate (91 %) for SOD-like activity and a conversion rate of 84 % to scavenging of H_2O_2 and V_{max} of 69.085 mg L^{-1} min^{-1} to oxygen generating for catalase-like activity. Accordingly, RNP can reduce ROS-driven cellular apoptosis of human umbilical vein endothelial cells (HUVECs), create a reparative microenvironment by inhibiting inflammation, and stimulate vascular regeneration. Furthermore, the RNP biotube demonstrates strong arterial repair in a rat model of arterial injury *in vivo*. This innovative approach highlights the capability of RNP biotubes as an effective approach for ROS-scavenging and anti-inflammatory vascular therapies.

2. Experimental section

2.1. Synthetic procedure of biomaterials

2.1.1. NiMOF nanosheets

First, $Ni(OAc)_2{\cdot}4H_2O$ (0.4 mmol, 99.2 mg) was dissolved in 24 mL H_2O. 1,4-H_2BDC (0.2 mmol, 33.2 mg) was dissolved in 24 mL DMAC. Afterward, the two solutions were mixed with stirring, transferred into a 100 mL autoclave, and reacted at 150 °C for 3 h. After centrifugation, the products underwent washing steps using deionized H_2O and ethanol. Finally, NiMOFs were dried in a vacuum oven at 60 °C for 12 h.

2.1.2. RN

44 mg NiMOF was ultrasonically dispersed in 40 mL H_2O for 1 h. 4.1 mg $RuCl_3{\cdot}3H_2O$ was added to the NiMOF suspension and stirred at 30 °C for 12 h. The products were collected by the same procedure as for NiMOF.

2.1.3. RNP

100 mg of RN was dispersed in 5 mL of hexafluoroisopropanol and stirred for 30 min. Then, 750 mg of PCL was added, and the mixture was magnetically stirred for 12 h at room temperature to prepare the electrospun solution. A series of RNP samples with varying RN doping ratios (RN:PCL = 1:10, 1:7.5, 1:5, and 1:2.5) were prepared by adjusting the RN content, which were labeled as $RNP_{1/10}$, $RNP_{1/7.5}$, $RNP_{1/5}$, and $RNP_{1/2.5}$, respectively. After evaluation, the $RNP_{1/7.5}$ composition was chosen for further research and simply referred to as RNP in later experiments. RNP was fabricated by an electrospinning device at a total voltage of 16 kV and a flow rate of 2 mL h^{-1}. The metal ions release efficiency in PBS solutions for different days, and was calculated as follows: efficiency% = $C_{measured}/C_{Total} \times 100$ %.

2.2. Catalase-like catalytic activity test

2.2.1. DPPH· scavenging test

The total radical scavenging ability of the biocatalyst was demonstrated by using 1,1-diphenyl-2-picrylhydrazyl radical (DPPH·). Then, the absorbance at $\lambda_{max} = 519$ nm was tested after the mixture had reacted for 30 min. The concentration effects of RNP (2.5, 5, 7.5, and 10 mg per 2 mL) on DPPH·scavenging properties were also analyzed.

2.2.2. $\cdot O_2^-$ scavenging test

O_2^- was generated *in situ* by dissolving KO_2 (1 mg) in dimethyl sulfoxide solution (DMSO) (1 mL) containing 18-crown-6-ether (3 mg mL^{-1}). Following the addition of RNP and 5-min reaction, the remaining $\cdot O_2^-$ was detected using nitroblue tetrazolium (NBT) (10 μL, 10 mg mL^{-1} in DMSO). Scavenging activity was calculated from the absorbance difference at 680 nm versus the control.

2.2.3. CAT-like Tests-H_2O_2 elimination

The H_2O_2 scavenging activity was measured by reacting 10 mM H_2O_2 with 10 mg biocatalysts in 2 mL PBS (pH 7.4). At each time point, 50 μL of the reaction mixture was combined with 100 μL $Ti(SO_4)_2$ solution (13.9 mM), and the absorbance at 405 nm was measured every 10 min for 60 min. The final absorbance reading at 60 min determined the H_2O_2 scavenging efficiency. Different RNP concentrations (2.5, 5, 7.5, and 10 mg per 2 mL) were tested to demonstrate the concentration-dependent H_2O_2 removal effect.

2.2.4. CAT-like Tests-O_2 generation assay

100 mM H_2O_2 and 20 mg RNP were combined in 20 mL PBS (pH 7.4), followed by measuring the O_2 concentration using a dissolved oxygen meter (INESA, JPSJ-605 F) every 5 s until 300 s. To analyze the biocatalytic kinetics of O_2 generation, 20 mg of biocatalysts and H_2O_2 with concentration gradients (50, 100, 150, 200, 300, 400, and 500 mM, respectively) were dissolved in PBS to a final volume of 20 mL. The O_2 concentration was then measured every 5 s for 100 s. The O_2 generation rates were plotted against their corresponding H_2O_2 concentration and were analyzed by fitting to the Michaelis-Menten kinetic equation $V = (V_{max} \times [S])/(K_m + [S])$. Furthermore, a double-reciprocal Lineweaver–Burk plot (Equation $(1)/v = K_m/V_{max} \times 1/[S] + 1/V_{max}$) was constructed to calculate the Michaelis constant (K_m) and maximal reaction velocity (V_{max}). Among them, V_{max} is the maximum reaction rate in the ROS catalytic reaction; The measured K_m suggests the enzyme-substrate affinity, where lower K_m values indicate stronger binding affinity, and [S] is the concentration of H_2O_2. The oxygen production rate was calculated as (O_2 production of the material at 300 s – O_2 production of the blank control at 300 s)/time.

2.3. Hemocompatibility

2.3.1. Blood count assay in vitro

1×1 cm^2-sized PCL and RNP were individually exposed to 400 μL freshly anticoagulated whole blood for 30 min. Post-incubation hematological analysis was conducted using a Mindray BC-5100 analyzer. PCL and RNP were first incubated in 400 μL whole blood for blood count analysis. After two 200 μL platelet-poor plasma (PPP) washes with intermediate solution collection, the remaining blood cell levels on the materials were determined.

2.3.2. Red blood cells (RBCs) morphology and hemolysis assessment

After a 1:1 PB S dilution of anticoagulated blood, RBCs were purified through centrifugation (644×*g*, 10 min) and washed five times. Morphological examination and hemolytic analysis were then performed. Subsequently, a 1 mL RBC suspension was incubated with PCL and RNP at 37 °C. Deionized water and PBS served as the positive and negative controls, respectively. After a 3 h incubation, the suspension underwent centrifugation at 10,304×*g* for 3 min. The supernatant was collected for analysis, with RBCs morphology characterized by SEM. Hemoglobin release was quantified by measuring the absorbance of the supernatant at 540 nm using a UV-1750 spectrophotometer (Shimadzu). The hemolysis percentage was calculated as:

$$\text{Hemolysis ratio } (\%) = 100 \times (A_s - A_n) \big/ (A_p - A_n)$$

where A_s, A_p, and A represent the absorbances of test samples, negative control (PBS), and positive control (deionized water), respectively. Triplicate measurements (mean ± SD, n = 3) ensured data reliability.

2.4. C3a and C5a generation

There is a close link between coagulation and complement systems, and thrombus generation often leads to complement activation. The levels of C3a and C5a generation were detected by ELISA (Fisher Scientific) in human whole blood anticoagulated by hirudin (300 IU·mL^{-1} of blood, HYPHEN BioMed) and sodium citrate synergistically. 200 μL of whole blood was introduced into PP tubes with PCL or RNP. After that, 8 mM $CaCl_2$ and 6 mM $MgCl_2$ (final concentration) were added to trigger the complement activation, using Cobra Venom Factor (CVF) as the positive control (final concentration of 1 μg mL^{-1}, Quidel Corporation), and the negative control group was an untreated blank control group. After being incubated for 30 min at 37 °C, the whole blood was stopped by adding EDTA (final concentration of 10 mM) and then centrifuged for 10 min at 2500 g to obtain plasma. Finally, the detections were conducted according to the respective instruction manuals. At least three parallel sample groups were applied to get a reliable value, and the results were expressed as mean ± SD.

2.5. Cell culture

HUVECs were maintained in complete growth medium consisting of DMEM (Gibco, China) plus 10 % FBS (Gibco, Australia) and 1 % penicillin-streptomycin at 37 °C in 5 % CO_2. 3D vascular cell culture was conducted as follows: RNP and PCL biotubes were cut to ~1.5 cm and sterilized. HUVECs were expanded to ~70 % confluence in 60 mm Petri dishes, detached by trypsinization, resuspended in 1 mL medium, and transferred into 1.5 mL sterilized centrifuge tubes containing the biotubes. The suspension readily infiltrated the porous tube wall, allowing HUVECs to adhere and spread along the surface.

2.6. In vitro cytotoxicity

The HUVECs were seeded in 24-well plates (2×10^5 cells·mL^{-1}) for 24 h. Using the Calcein-AM/PI double-staining kit (Beyotime, China) to detect cell viability.

2.7. Flow cytometry for cell apoptosis analysis

HUVEC suspensions (2×10^4 cells·mL^{-1}) were seeded into 24-well plates and incubated overnight. Then, cells were co-incubated with 200 μM H_2O_2 and PCL or RNP. Apoptotic cells were identified by Annexin V-FITC/PI double staining (Yeasen, China) and quantified by flow cytometry.

2.8. Intracellular ROS generation

Intracellular ROS levels were measured using DCFH-DA, which was used as the probe to detect intracellular ROS. HUVECs (2×10^5 cells/well) were seeded in 24-well plates and pre-cultured for 12 h (37 °C, 5 % CO_2). RNP was cut to a 1×1 cm^2 size, then coincubated with cells for another 12 h. After PBS washing, cells were incubated with 10 μM DCFH-DA in serum-free DMEM (37 °C, 1 h, dark). Then, the intracellular ROS-scavenging ability of biocatalysts was qualitatively and quantitatively evaluated by flow cytometry and an automated inverted fluorescence microscope (Olympus IX83, Japan), respectively.

2.9. Cell wound scratch assay

HUVECs were seeded in 6-well plates, and a serum-free medium was used to minimize the effects of serum on cell proliferation. Then a vertical line was drawn with the 200-μL micropipette tip over the ruler. The cells were washed with PBS, photographed under a microscope (FV2000, Olympus, Japan), and then placed at 37 °C in a 5 % CO_2 incubator. The wound closure rates were counted by using the ImageJ program (Media Cybernetics, Rockville, USA).

2.10. Immunofluorescence staining

After PBS rinses, fixation was performed using 4 % paraformaldehyde (Biosharp) for 15 min. Cells were permeabilized (0.1 % Triton X-100/PBS, 10 min) and rinsed with PBS. After blocking (10 % goat serum, 40 min), samples were stained with fluorescent antibodies (1 % BSA/PBS) for 2 h. For indirect staining, cells were coincubated overnight with the primary antibody at 4 °C. After rinsing with PBS, cells were stained with DAPI and secondary antibodies in the dark for 30 min. Immunofluorescence images were obtained by confocal microscopy (Leica St5). Primary antibodies were used: rabbit polyclonal *anti*-Vinculin (Solarbio, K106900P, 1:100 dilution) and *anti*-Zonula Occludens-1, ZO-1 (ab96587, Abcam, USA). Secondary antibodies used were goat anti-mouse IgG Alexa Fluor 647 (Yeasen, 33213ES60, 1:100 dilution) and goat anti-rabbit IgG Alexa Fluor 647 (Yeasen, 33213ES60, 1:100 dilution). Focal adhesions were identified based on punctate morphology, co-localization with F-actin termini, and Vinculin fluorescence intensity as an indicator of adhesion maturity.

2.11. In vivo experiments

Eight-week-old male SD rats were purchased from the Experimental Animal Center of Sichuan University. The animal experiments were conducted following the Sichuan University Animal Ethics Committee-approved procedure. The rats were randomly assigned to three groups: 1) Sham group, 2) PCL group, and 3) RNP group. Rats were shaved on their abdomen. After skin disinfection, a scalpel was used to cut through the skin and the muscular layer of the rat to expose the abdominal cavity. The intestine was carefully pushed to one side to expose the abdominal aorta. The abdominal aorta, within 1 cm below the left renal vein, was chosen as the target experiment site. The mucosa between the abdominal aorta and inferior vena cava of all groups was separated, and the aorta was punctured to cause wound inflammation. As a control, the operation of the Sham group was finished without punching holes, while the PCL and RNP groups both punched to create the injured rat model. Then, artificial biotubes were wrapped around the injured artery and sutured to prevent leakage and failure. Rats were sacrificed 7 days after the operation. Before the surgery, conventional ultrasound and color Doppler ultrasound were used to show the condition of the arterial vessels. The treated arteries were cut off and fixed in a 3.7 % formaldehyde solution for H&E, Masson trichrome, TNF-α, CD68, iNOS, IL-10, α-SMA, VEGF, and CD31 staining. Meanwhile, the blood of the rats was drawn for complete blood count and serum biochemical analysis.

2.12. Statistical analysis

All statistical analyses were conducted using GraphPad Prism. Data are shown as the mean ± standard deviation (SD). Error bars were derived from the experiment repeated at least three times. For the comparison of multiple groups, the one-way analysis of variance (ANOVA) was used. $^*p < 0.05$ indicates statistically significant. $^*p < 0.05$, $^{**}p < 0.01$, $^{***}p < 0.001$, $^{****}p < 0.0001$ were regarded as statistically significant.

3. Results and discussion

3.1. Preparation and structural characterization of RN biocatalyst

The RN biocatalyst, featuring an active Ru–O–Ni interface, is synthesized through a facile two-step reaction (Fig. 1a). First, the pristine $[Ni_3(OH)_2(C_8H_4O_4)_2(H_2O)_4]\cdot 2H_2O$ (termed as NiMOF) with abundant hydroxyl groups has been prepared by hydrothermal reaction of 2-hydroxy-1,4-benzenedicarboxylic acid (1,4-H_2BDC) and nickel acetate tetrahydrate ($Ni(OAc)_2\cdot 4H_2O$). Then, the introduction of Ru species is conducted by mixing a certain amount of ruthenium chloride hydrate ($RuCl_3\cdot 3H_2O$) and NiMOF to form Ru nanocluster anchored NiMOF (RN)

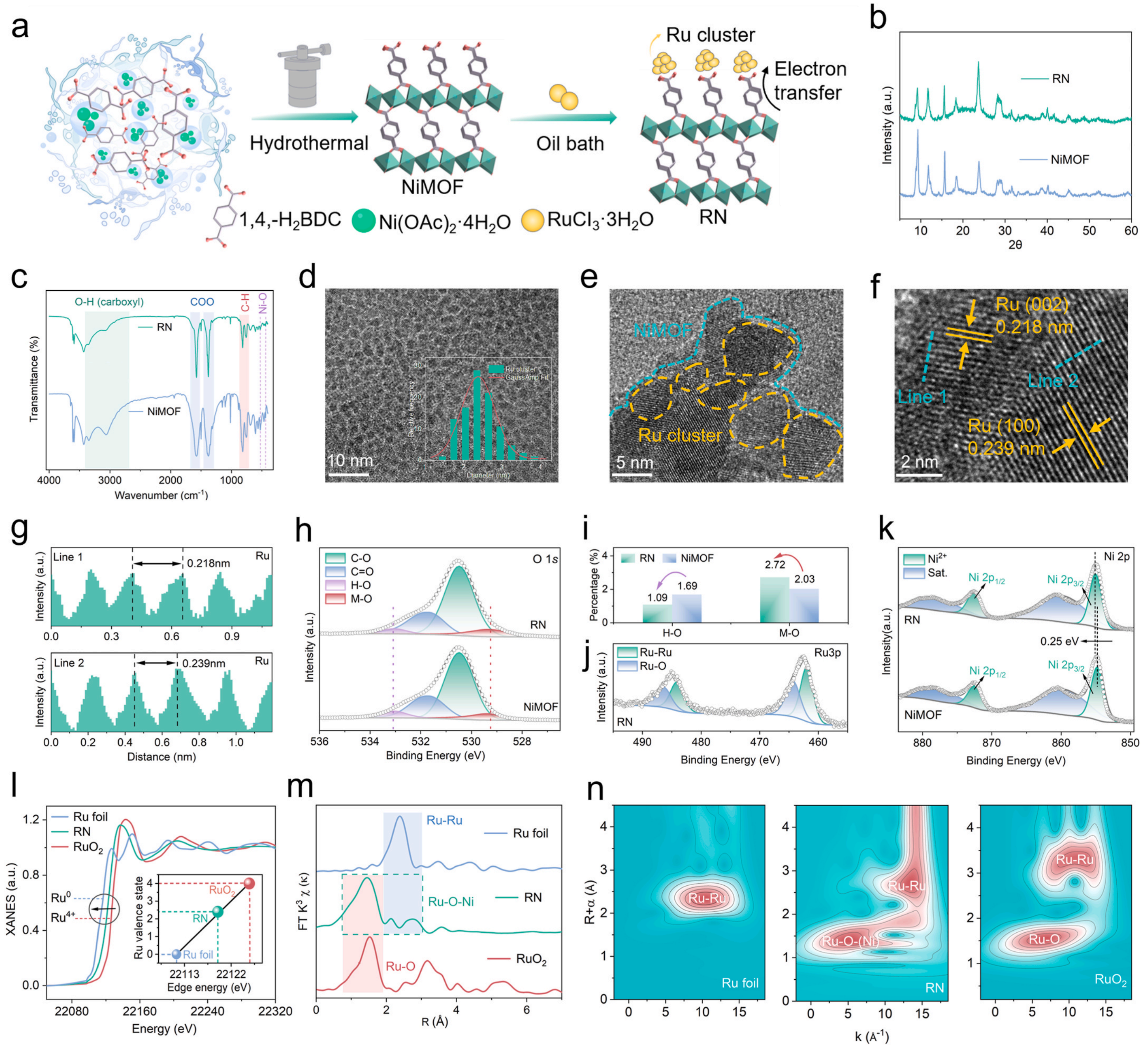

Fig. 1. Synthetic diagram and structural characterization of RN biocatalyst. (a) Schematic illustration of the RN formation. (b) Powder XRD patterns of NiMOF and RN. (c) FT-IR patterns of NiMOF and RN. (*d*–f) HRTEM image of RN. (g) Lattice line scanning analyses of RN. High-resolution XPS regions of RN: (h) O 1s, (i) The H–O and *M* − O distribution proportion corresponding to (h), (j) Ru 3*p*, and (k) Ni 2*p*. (l) XANES spectra at the Ru *K*-edge and average valence states of RN, Ru foil, and RuO$_2$. (m) The Ru k^2-weighted Fourier transforms for RN, Ru foil, and RuO$_2$. (n) Wavelet-transform images of Ru *K*-edge EXAFS of Ru foil, RN, and RuO$_2$.

catalysts. Powder X-ray diffraction (XRD) patterns show that the RN bears similar diffraction patterns as the pristine NiMOF (CCDC No.638866, triclinic system, space group *P*-1), indicating that the crystal structure of MOF is retained after Ru incorporation (Fig. 1b) [60,61]. The Brunauer-Emmett-Teller (BET) analysis (Fig. S1) reveals that RN (29.993 m^2 g^{-1}) exhibits a higher surface area compared to NiMOF (17.891 m^2 g^{-1}), suggesting the potential exposure of more active sites on its surface.

Furthermore, the Fourier transform infrared spectrum (FT-IR) gives chemical structural information of NiMOF and RN (Fig. 1c). Firstly, the stretching vibrations of ν_{as} (–COO−)/ν_s (–COO−) (1574 and 1378 cm^{-1}) and C–H stretching bands (815 and 752 cm^{-1}) can be observed in both NiMOF and RN, which corresponds to the characteristic peaks of the BDC ligand in NiMOF [62]. Meanwhile, the Ni–O stretching vibration at 526 cm^{-1} and in-plane Ni–O–H bending vibration at 440 cm^{-1} of NiMOF and RN can be found as well [63]. Notably, the stretching vibration peak of the O–H bond between 3300 and 2500 cm^{-1} in RN decreased after doping of Ru species, suggesting that Ru ions have successfully undergone ion exchange with the O–H at the carboxyl terminus of NiMOF, which indicates the successful formation of Ru–O–Ni interface on RN.

The morphologies of the synthesized RN are analyzed through scanning electron microscope (SEM) and transmission electron microscope (TEM). The SEM and TEM images reveal that Ru nanoclusters, with an average diameter of approximately 2.3 nm, are uniformly anchored on the surface of NiMOF nanosheets (Figs. 1d, e, S2-3). High-resolution TEM (HRTEM) images display well-defined lattice fringes with a spacing of 1.04 nm, assignable to the (200) plane of NiMOF (Fig. S4) [64]. Meanwhile, Fig. 1f reveals interplanar spacings of 0.218

nm and 0.239 nm, corresponding to the (002) and (100) planes of Ru nanoclusters (JCPDS No. 06–0663), consistent with the lattice line scanning analysis shown in Fig. 1g [65]. Moreover, the energy-dispersive X-ray (EDS) mapping images show that Ni atoms are uniformly dispersed in RN, and the distribution of Ru element confirms the formation of Ru clusters (Figs. S5–6) [66].

The XPS survey scans of RN show obvious Ru, Ni, C, and O signals, while no Ru signals are exhibited in the pristine NiMOF (Fig. S7 and Table S1). The high-resolution O1*s* spectrum of RN and NiMOF can both be divided into four peaks with their binding energies at 529.3, 530.5, 531.7, and 533.05 eV, assigned to the metal oxides (M − O), O–C, O═C, and O–H, respectively (Fig. 1h and Table S2). Notably, the decreased O–H species (1.09 at%) and increased M − O species (2.72 %) of RN has been observed, when compared to that of pristine NiMOF with 1.69 % O–H and 2.03 % M − O species, which demonstrates that the Ru clusters are anchored to the NiMOF by substituting carboxyl-terminal H–O groups with Ru to form stable Ru–O bonds (Fig. 1i) [64]. The high-resolution Ru 3*p* spectrum of RN in Fig. 1j can be deconvoluted into metallic Ru (461.96 and 484.10 eV) and oxidative Ru species (464.27 and 486.42 eV), providing compelling evidence for the successful formation of the Ru–O–Ni interface between the Ru nanocluster and the NiMOF, which implies that electrons can migrate through the oxygen-containing functional group [67–69]. Meanwhile, the binding energies of 282.04 eV and 286.95 eV in the high-resolution C 1*s* spectrum can be attributed to Ru $3d_{5/2}$ and Ru $3d_{3/2}$, respectively, due to the overlap of the binding energies of C 1*s* and Ru 3*d* (Fig. S8). Moreover, the high-resolution Ni 2*p* spectrum of RN shows the characteristic peaks of Ni^{2+} at a binding energy of 854.85 and 872.33 eV (Fig. 1k), which is higher than that of NiMOF, indicating the electron transfer from NiMOF to Ru clusters through the Ru–O–Ni interface [70–72].

To explore the coordination microenvironments and electronic configurations of RN biocatalysts in detail, X-ray absorption near-edge structure (XANES) and extended X-ray absorption fine structure (EXAFS) spectroscopies have been conducted. The Ru *K*-edge XANES spectra show that the pre-edge peak in RN is located between Ru foil and RuO_2, indicating that the valence state of Ru is between 0 and +4 [66, 68], and the valence analysis shows that the average valence of Ru in RN is +2.4, which is consistent with the XPS results (Fig. 1l). Furthermore, the EXAFS spectrum of RN exhibits one major peak belonging to the Ru–O-(Ni) bond around 1.5 Å and two additional coordination peaks attributed to the Ru–Ru metal bond around 2.0–3.0 Å, primarily demonstrating the formation of the Ru–O–Ni interface and Ru

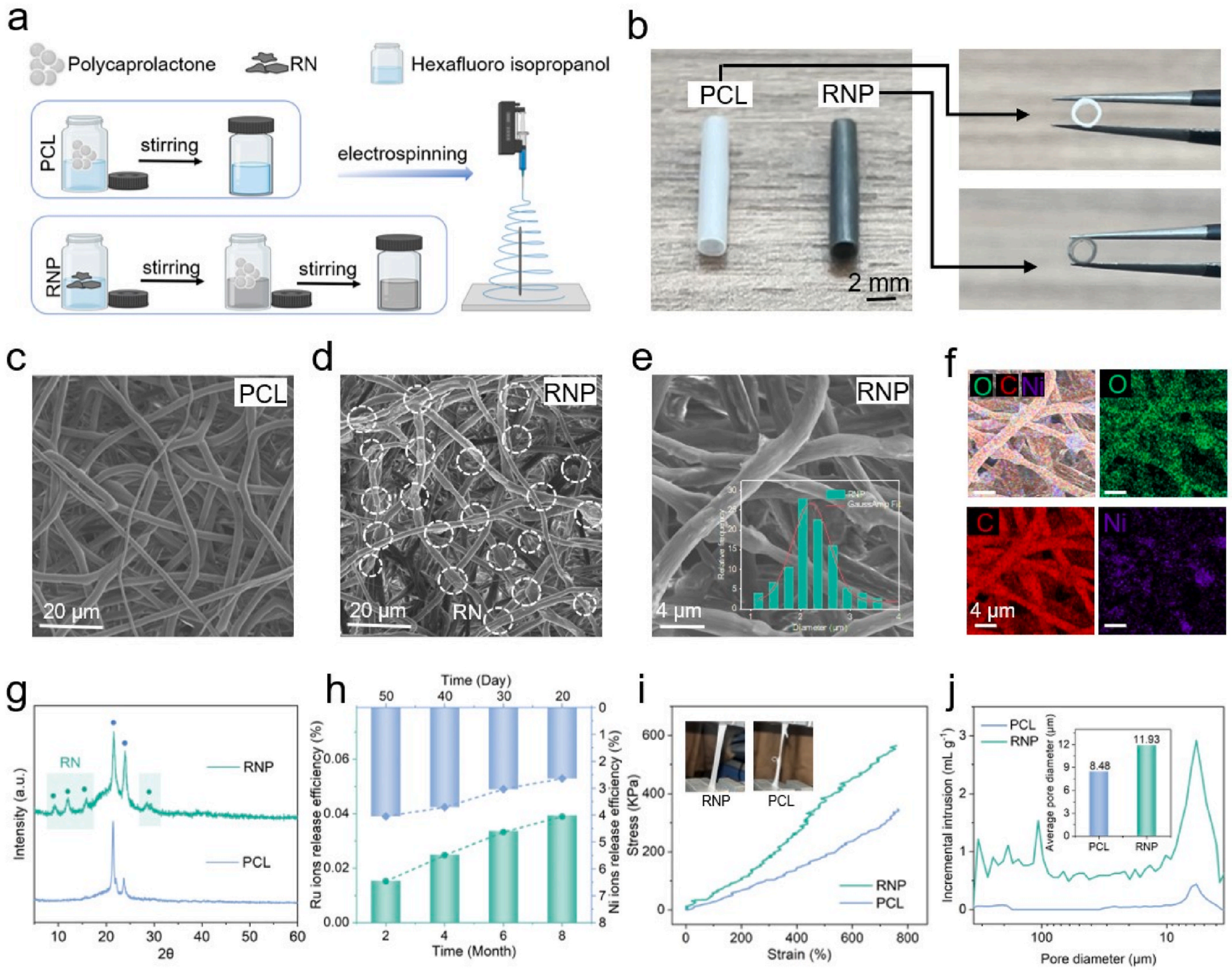

Fig. 2. Morphology and structural characterization of RNP biotubes. (a) Schematic illustration of the fabrication of RNP. (b) Macroscopic view of PCL and RNP artificial biotubes. (c, d) SEM images and (e) size distribution of fiber diameter of RNP. (f) EDS mapping images of RNP. (g) XRD patterns of PCL and RNP. (h) The metal ion release efficiency varies over different time periods. (i) Stress–strain curves of PCL and RNP. (j) Porosity and pore diameter analyses of PCL and RNP from MIP.

nanoclusters (Fig. 1m), which is also consistent with the corresponding wavelet-transform (WT) results (Fig. 1n). In summary, the Ru–O–Ni interface and potent interfacial charge transfer between Ru nanoclusters and NiMOF supports may facilitate the interface stability and redox potential of RN materials and even the artificial biotubes.

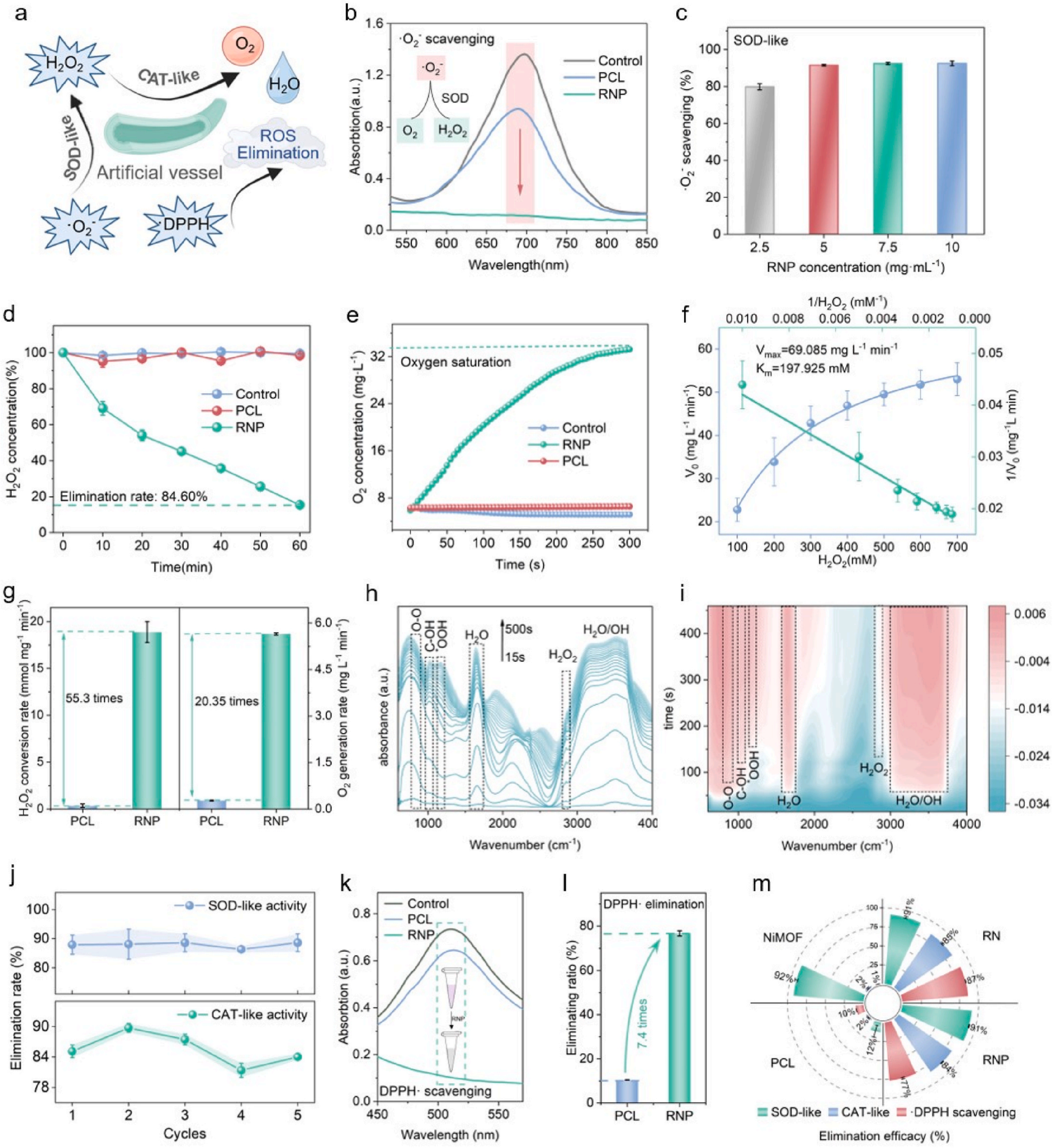

Fig. 3. Biocatalytic ROS-elimination properties of RNP. (a) Schematic depiction of the cascade SOD-CAT and DPPH· biocatalytic capability of RNP. (b) SOD-like performance for scavenging of $\cdot O_2^-$. (c) SOD-like activities of RNP at different concentrations. (d) H_2O_2 elimination activity. (e) O_2 generation ability. (f) Double-reciprocal plots are used to determine the kinetic constants of RNP with H_2O_2 as the substrate. (g) H_2O_2 conversion rates and O_2 generation rates of PCL and RNP biocatalysts. (h) *In-situ* FT-IR spectrum and (i) the corresponding contour plot of RNP for H_2O_2 decomposition. (j) Cycling activities of SOD and CAT for RNP. (k) DPPH· scavenging properties, and (l) DPPH· scavenging rates of PCL and RNP. (m) Radial column chart of biocatalytic ROS-elimination properties. The control group was an untreated blank control group.

3.2. Fabrication and characterization of RNP biotubes

After successfully engineering the RN biocatalyst, we further integrated the promising antioxidase mimic onto a PCL fiber scaffold. As shown in Fig. 2a, we prepare the mixed RN and PCL electrospinning solution to construct the artificial biocatalytic biotubes. To optimize the morphology and antioxidase-like performance, different ratios of RN were introduced during the synthesis of RNP. Notably, at an RN to PCL mass ratio of 1:7.5, the resulting RNP exhibits the uniform morphology and cost-effective, optimized CAT-like activity (Figs. S9–11). Therefore, unless otherwise specified, the RNP in the following section refers to the material obtained at a 1:7.5 mass ratio. Additionally, the bare PCL biotube without RN is obtained as the control group.

The overview indicated that PCL and RNP have an inner diameter of 2 mm and exhibit a color change after introducing RN biocatalysts (Fig. 2b). The morphologies of bare PCL and RNP are presented in the SEM images (Fig. 2c–f, Fig. S12, 13). The RN nanosheets can be observed on the PCL fibers after electrospinning, and the fiber diameter of RNP with 2.1 μm is slightly smaller than that of bare PCL (2.5 μm). This decrease in fiber diameter following antioxidant incorporation is consistent with a previous study [73]. Then, powder XRD was conducted to analyze the crystal structures of the prepared biotubes, and RNP contained characteristic peaks of both RN and PCL (Fig. 2g). Similarly, FT-IR, Raman, and XPS spectra have been utilized to validate the successful integration of RN onto PCL from both structural and chemical characterizations (Figs. S14–16).

Given that the sustained drug release profile and mechanical strength of the biotube are of utmost significance, we conducted a further assessment of the corresponding effects on RNP. The release profile of metal ions from RNP in PBS solution not only confirms the presence of Ru and Ni but also demonstrates a remarkably slow degradation rate, suggesting its potential for sustained long-term therapeutic efficacy (Fig. 2h). Then the mechanical analysis shows the characteristic tensile stress-strain curve on the artificial biotubes (Fig. 2i), and the corresponding Young's modulus and tensile strength are subsequently calculated. As shown in Fig. S17, the RNP exhibits a higher mechanical strength than bare PCL, suggesting that RNP can achieve the mechanical requirements of vascular grafts. This enhancement is attributed to interfacial reinforcement via polymer chain interlocking with MOF particles [74]. In addition, Low porosity in tissue-engineered vascular scaffolds impedes cellular infiltration and nutrient diffusion, leading to delayed tissue regeneration [75]. Therefore, we employ mercury intrusion porosimetry (MIP) to evaluate the pore diameter distributions of PCL and RNP biotubes. As shown in Fig. 2j, RNP exhibits a larger average pore diameter (11.93 μm) compared to PCL (8.48 μm), which facilitates enhanced cellular infiltration and vascularization. Moreover, tailored artificial biotubes with targeted strength can be manufactured through modulating the wall density and thickness to accommodate the needs of different vessel types and application conditions (Fig. S18).

3.3. Antioxidase-mimetic activities of artificial biotubes

After characterizing the chemical and morphological structure of artificial RNP biotubes, their biocatalytic ROS elimination properties are systematically investigated (Fig. 3a). Initially, the antioxidative activities of RN and pristine NiMOF are evaluated. The $\cdot O_2^-$ scavenging activity of RN is similar to that of NiMOF, demonstrating SOD-like performance attributed to the Ni catalytic sites, with an outstanding elimination rate of 86.3 % at a concentration of 10 μg mL^{-1} (Fig. S19). After introducing Ru species, RN exhibits significantly enhanced CAT-like activity compared to pristine NiMOF, particularly regarding H_2O_2 elimination and oxygen generation (Figs. S20 and 21). Additionally, general antioxidative activities are measured utilizing the DPPH· radical assay. The RN exhibits efficient and continuous free radical scavenging capabilities, outperforming pristine NiMOF, which can benefit from the formation of a Ru–O–Ni interface with fast charge transfer (Fig. S22).

After evaluating the antioxidase-mimicking performance of RN biocatalysts, the detailed *anti*-ROS capabilities of artificial biotube RNP have been further assessed (Fig. 3a). As the first step of the SOD-CAT cascade for ROS-scavenging ($\cdot O_2^-$ to H_2O_2), the SOD-like property of RNP is determined by the scavenging efficiency of $\cdot O_2^-$ using NBT as a selective indicator [76]. Compared to bare PCL, RNP displays impressive and dose-dependent inhibition of $\cdot O_2^-$ radical (Fig. 3b and c). The second pivotal step in the ROS-eliminating cascade, CAT-like activity, is examined. PCL shows minimal H_2O_2 removal ability, while RNP achieves a high removal efficiency of 84.60 % in 60 min (Fig. 3d and Fig. S23, 24). Furthermore, O_2 generation tests verify that the RNP biocatalytic biotube effectively decomposes the H_2O_2 substrate to produce substantial O_2 (Fig. 3e).

The steady-state catalytic kinetics of the CAT-mimetic process are determined using H_2O_2 as the substrate, and a linear double-reciprocal plot has been employed to calculate the Michaelis constant (K_m) and maximal reaction velocity (V_{max}). As detailed in Equations of the 2.2.4, the K_m and V_{max} for the RNP biocatalyst are calculated to be 197.925 mM and 69.085 mg L^{-1} min^{-1}, respectively (Fig. 3f). In addition, H_2O_2 conversion and O_2 generation rates further support the efficient consumption of H_2O_2 by RNP (Fig. 3g), leading to the generation of O_2, highlighting the outstanding CAT-like activity of RNP. *In-situ* FTIR has been utilized to track the intermediate changes during the CAT process. As shown in Fig. 3h and i, the rapid OH species adsorption (1030 cm^{-1}), typical formation of the *OOH intermediate (1157 cm^{-1}), and a large amount of O_2 (829 cm^{-1}) and H_2O (1640 cm^{-1}) products accumulation has been observed during the decomposition process of H_2O_2 [77–81]. A stability test was conducted to evaluate the long-term stability of the SOD-CAT cascade system. Remarkably, the catalytic performance shows no significant decline after five cycles, indicating that RNP maintains excellent stability during ROS elimination (Fig. 3j). The DPPH· assay has also been performed. RNP exhibited 7.4 times higher performance than that of bare PCL in inhibition of the DPPH· radical (Fig. 3k, l, Fig. S25). The above biocatalytic profiles of NiMOF, RN, PCL, and RNP are summarized in Fig. 3m, confirming the excellent cascade-like and antioxidant catalytic activity of RNP biotube, which can serve as a promising candidate for biomedical applications.

3.4. In vitro biocompatibility and ROS damage defense of HUVEC cells via RNP

Having established that RNP functions as an effective antioxidase-like biotube with extensive and potent ROS scavenging abilities, we then carefully examined its blood compatibility and potential in protecting HUVECs in high-ROS-level microenvironments to investigate its clinical utility as an artificial biotube (Fig. 4a).

Firstly, the blood compatibility of RNP biocatalytic biotubes has been evaluated to compare with bare PCL, which has obtained safety certifications from several health regulatory authorities due to its excellent biodegradability, biosafety, and blood compatibility [82,83]. Complete blood count *in vitro* shows negligible changes in RBCs, white blood cells (WBCs), and platelets for both the PCL and RNP groups, suggesting the stable blood component (Fig. 4b, Fig. S26, and Table S3). To assess the affinity for red blood cells (RBCs) post-incubating with biotubes, hemolysis experiments were conducted, and no obvious hemolysis could be observed for the two biotubes (Fig. 4c). Meanwhile, upon centrifugation, the clear and colorless supernatant demonstrates no significant RBC damage or release of hemoglobin (Fig. 4d). SEM images of the harvested RBCs show characteristic biconcave shapes (Fig. 4e, Fig. S27). These results suggest that the RNP has good blood compatibility as bare PCL. In addition, to evaluate the impact of RNP on blood coagulation, comprehensive plasma coagulation tests have been conducted. The clotting times of platelet-poor plasma (PPP) incubated with PCL and RNP were detected, respectively, containing activated partial thromboplastin time (aPTT), prothrombin time (PT), and thrombin time (TT), and all display negligible changes both in PCL and

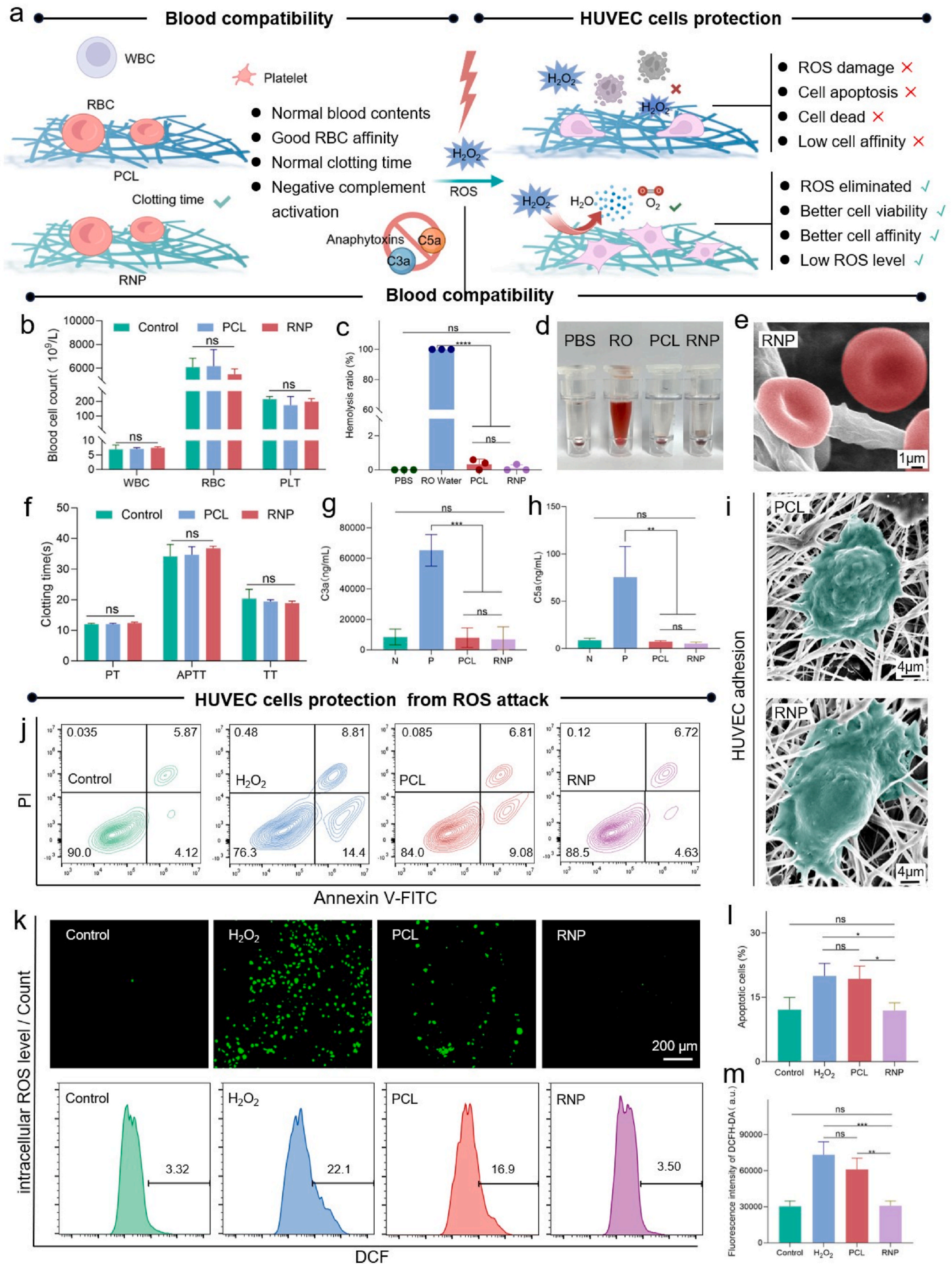

(caption on next page)

Fig. 4. Blood compatibility and HUVEC cells protection from ROS attack via RNP artificial antioxidase-mimicking biotube. (a) Schematic depiction of RNP for suppressing oxidative damage. (b) Blood cell count for untreated blood and blood post-incubation with PCL and RNP. (c) Hemolysis ratio of the blood post-incubation with PCL and RNP. (d) Digital photos of supernatants (upper) obtained by centrifugation of the salvaged blood. RO: RO water treated. (e) Adhered RBCs retained their typical cell morphologies on RNP. (f) Clotting times after incubation with PCL and RNP for 30 min. Emergence of (g) C3a and (h) C5a in the blood post-incubation with PCL and RNP. N and P refer to the negative and positive control groups, respectively. (i) HUVECs spread on PCL and RNP. (j) Flowcytometric apoptosis detected by Annexin V-FITC/PI fluorescence staining of HUVECs incubated with PCL and RNP. (k) Fluorescence images and flow cytometry data of DCFH-DA staining. (l) Quantitative analysis of cells after Annexin V-FITC/PI staining with biocatalysts from (h). (m) Quantitative assessment of cells by DCFH-DA fluorescence staining with biotubes from (i). H_2O_2: cells pretreated with 200 μM H_2O_2; PCL and RNP: cells pretreated with 200 μM H_2O_2 and coincubated with the corresponding biocatalyst. Data are presented as mean ± SD from independent replicates ($n \geq 3$). n. s., non-significant were assessed by one-way ANOVA. The control group was an untreated blank control group.

RNP (Fig. 4f). Complement activation can cause an increase in complement anaphylatoxins such as C3a and C5a in the serum; thus, the effect of biotubes on complement activation has also been investigated. For both biotubes, the produced C3a and C5a exhibited little differences relative to untreated blood, indicating that the complement cascade is not activated in the blood collected (Fig. 4g and h). The above results indicate that, as artificial biological tubes, RNP exhibits excellent blood compatibility and demonstrates great potential in the field of vascular tissue engineering.

After validating the excellent blood compatibility of artificial biotubes, we have systematically assessed their HUVECs protection ability. Firstly, the biocompatibilities have been evaluated. The growing cells are tightly adhered to both biotubes, as shown in SEM images (Fig. 4i). HUVECs were mostly spherical with less spreading on PCL, while the cells on the RNP showed spreading and elongated morphology. Meanwhile, cells on both biotubes exhibit considerable viability, as indicated by live/dead assays (Fig. S28). Then, the cell protection ability of the biotubes has been evaluated in ROS conditions (200 μM H_2O_2). Flow cytometric apoptosis detection by Annexin V-FITC/PI staining demonstrates that RNP can significantly reduce ROS-induced apoptosis to a rate of 12.17 %, which is consistent with the control group level (11.93 %) in 12 h, while the apoptosis rate of the PCL group reaches up to 19.32 % like the H_2O_2 group (19.98 %) (Fig. 4j–l). The Live/Dead staining demonstrates negligible cell death in the RNP samples and controls (Fig. S29). Next, we utilize the 2,7-dichlorofluorescein diacetate (DCFH-DA) to determine the intracellular ROS scavenging efficiency of HUVECs by the biotubes. Fig. 4k observes a distinct ROS fluorescence (green) in the 200 μM H_2O_2-treated group. In contrast, the ROS fluorescence intensity decreased under RNP treatment, demonstrating that RNP can efficiently eliminate intracellular ROS. Additionally, the quantitative assessment in Fig. 4m observes the lower ROS fluorescence intensity in the RNP and control group, while the PCL group presents much higher intracellular ROS. The above results demonstrate that the exceptional ROS scavenging ability of RNP allows it to modulate the fates of HUVECs under high oxidative stress conditions.

After verifying the biosafety and the effective ROS scavenging of the RNP biotube, we further evaluate its cell growth *in vitro*. High ROS levels will not only trigger apoptotic cell death but also impact the cytoskeletal alignment and the regulation of adhesion proteins, thus hindering cell motility, proliferation, and differentiation [84]. Therefore, to evaluate the effect of biotubes on cell migration in a high-level ROS condition, the wound-healing assay has been conducted through the coincubation of HUVECs with biotubes and the addition of 200 μM H_2O_2. Meanwhile, the bare PCL biotube is coincubated with HUVECs without H_2O_2 as the reference group. Compared to the PCL + H_2O_2 group (23.81 % wound closure at 24 h), the RNP + H_2O_2 group exhibits rapid healing progress, with up to 50.25 % closure at 24 h, which is similar to the PCL group (Fig. 5a–f). The aforementioned outcomes indicate that RNP can significantly promote cell migration under high ROS conditions.

Subsequently, we evaluate the effect of biotubes on the spreading and adhesion of HUVECs. Specifically, tiled PCL and RNP fiber materials are placed at the bottom of a 24-well plate to facilitate cell adhesion and growth on the fiber surface. As shown in Fig. 5b, the PCL + H_2O_2 group treated HUVECs exhibit abnormal cell spreading and morphology with a constricted form on the F-actin staining. In contrast, the RNP + H_2O_2 and PCL incubated HUVECs present larger outspread morphology (Fig. 5g). To assess changes in the cell spreading area, we examine the focal adhesion (FA) structures, which play a crucial role in regulating cell migration by connecting the actin cytoskeleton to the extracellular matrix. As depicted in Fig. 5b, HUVECs treated with PCL + H_2O_2 exhibit reduced vinculin protein expression, primarily localized around the nuclear region, suggesting weak adhesion to the PCL fiber under the elevated ROS levels. In contrast, the HUVECs co-incubated with RNP display a clear and spatially uniform distribution of FA, validating the improved cell adhesion to RNP fibers (Fig. 5h). These findings reveal that RNP significantly mitigates ROS-induced damage, thereby facilitating cytoskeleton modulation and strengthening cell adhesion.

In order to further evaluate the three-dimensional (3D) artificial biotubes, the growth of HUVECs on them is investigated. The sterilized biotubes were placed in the cell suspension, and PCL + H_2O_2 and RNP + H_2O_2 groups were added H_2O_2 to observe the growth of cells on the 3D biotubes in the ROS environment (Fig. 5c). After incubation in a fresh medium for 5 days, the biotubes underwent fluorescent staining and confocal imaging. As shown in Fig. 5d, the fluorescent images of live/dead staining show that the RNP + H_2O_2 and PCL groups show more cells and high viability for HUVECs (99.65 % and 99.64 %, respectively), while the PCL + H_2O_2-treated group presents fewer cells and a lower rate of cell living (95.6 %) (Fig. 5i).

Owing to the essential role of ZO-1 (a critical tight junction marker) in endothelial tissue, its localization has been analyzed in HUVECs grown on engineered biotubes over a 5-day period via immunofluorescence analysis to investigate endothelial development [85]. As shown in Fig. 5e, in terms of a longitudinal or cross-sectional view of the 3D biotubes, both RNP + H_2O_2 and PCL groups express abundant ZO-1 on the cytomembranes when compared to the PCL + H_2O_2 group, particularly at cell-cell junctions, indicating that RNP promotes the formation of an intact endothelial structure and a supportive microenvironment in seeded HUVECs. Moreover, further detailed quantitative analysis also proves the outstanding performance of RNP on cell protection from ROS attack (Fig. 5j).

3.5. *In vivo* vascular injury regeneration in rat model

After confirming the *in vitro* HUVEC-cell rescue activity of biocatalytic biotube, RNP was utilized as an artificial graft to replace the injured abdominal aorta in rat models with inflammatory disease to investigate its potential for *in vivo* application. Given the technical challenges associated with graft surgery in small animal models, the abdominal aorta was punctured to create a wound-induced inflammatory response. The detailed *in vivo* validation process is outlined as follows. The abdominal aorta, located 1 cm below the left renal vein, was selected as the target site for the experiment. The mucosa between the abdominal aorta and inferior vena cava was separated in all groups. As a control, the Sham group underwent the same procedure without puncturing the artery, while the PCL and RNP groups were subjected to arterial puncture to induce injury. The artificial biotubes were then wrapped around the injured artery and sutured to prevent leakage and failure. A schematic of the surgical procedure for *in vivo* implantation of PCL and RNP biotubes, along with optical images of the surgical site before abdominal suturing, is presented in Fig. 6a. The surgeries were

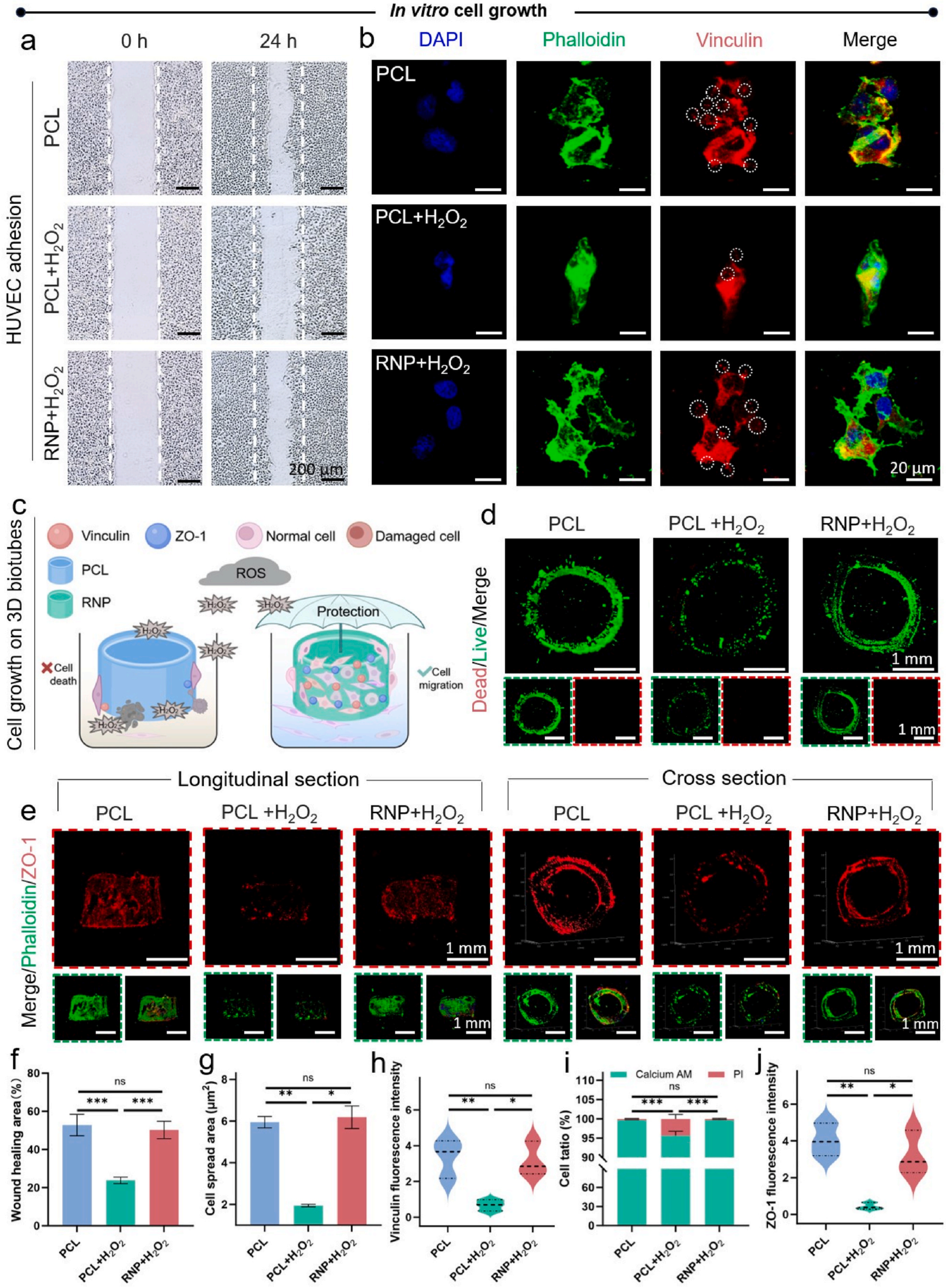

(caption on next page)

Fig. 5. ***In vitro* cell growth on 3D RNP artificial biotubes.** (a) HUVECs migrated into the wounded region were imaged by immunofluorescence microscopy at 0 and 24 h. (b) Phalloidin and Vinculin staining of HUVECs after different treatments. Dashed white circles highlight the representative vinculin-positive focal adhesion core regions. (c) Schematic illustration of HUVECs growing on three-dimensional artificial biotubes. (d) Representative Live/Dead cell staining (live cells: green, Dead cells: red) for HUVECs following different treatments. (e) The longitudinal and cross-section of the HUVEC-seeded 3D biotubes were incubated for 5 days. (f) Analysis of cell migration from a. (g) Analysis of cell spread area from b. (h) Analysis of Vinculin fluorescence intensity from b. (i) Analysis of Live/Dead cell fluorescent staining from d (j) Analysis of ZO-1 fluorescence intensity from e. PCL + H_2O_2 and RNP + H_2O_2: cells pretreated with 200 μM H_2O_2. Data are presented as mean ± SD from independent replicates ($n \geq 3$). n. s., non-significant were assessed by one-way ANOVA. (For interpretation of the references to color in this figure legend, the reader is referred to the Web version of this article.)

completed after abdominal suturing (Fig. S30).

7 days later, conventional ultrasound and color Doppler ultrasound imaging revealed that the arterial vessels in all groups remained continuous, with no abnormalities in the vascular walls and no defects in blood flow, indicating that no plaque, stenosis, or occlusion had occurred in the lumen of the blood vessels post-surgery (Fig. 6b and Fig. S31). Furthermore, the abdominal wall wound healing is consistent across all groups (Fig. 6c and Fig. S32), suggesting that the changes in inflammation-related markers between the groups are due to the arterial puncture rather than surgical wounds in the abdominal skin and musculature. To further investigate the surgical outcomes, the abdominal cavity was reopened on day 7 post-operation, and the level of adhesion in each group was assessed and scored quantitatively. For the PCL group, no white PCL vessels are visible due to severe adhesion, and the surgical site has been surrounded by intraperitoneal organs and tissue mucosa, along with dense neovascularization that is hard to remove (Fig. 6d and Fig. S33). Therefore, the clinical adhesion score for the PCL group is high at 2.7, whereas the RNP group does not exhibit any adhesion formation, resulting in a clinical adhesion score of 0, which is consistent with the Sham group (Fig. 6e and f). These findings clearly demonstrate that RNP is effective in preventing adhesion.

Under endothelial injury, platelet adhesion triggers thrombosis and inflammatory responses, promoting vascular smooth muscle cell proliferation and impairing endothelial repair [86–88]. Neutrophil accumulation at the injury site further exacerbates inflammation and delays healing [89]. These processes are reliably monitored through the circulating C-reactive protein (CRP), a stable inflammatory marker that reflects both acute and chronic inflammatory states [90]. On day 7 following surgery, the lymphocyte percentage (Lymph%), neutrophil percentage (Gran%), white blood cell (WBC) count, and CRP levels in the peripheral blood and plasma have been measured. The results for the RNP group are obviously lower than those for the PCL group and are consistent with the Sham group (Fig. 6g–k). These findings suggest that the RNP biotube, through its ROS-scavenging activity, effectively reduces inflammation caused by arterial puncture in rats.

After postoperative observation and hematological tests, we conducted pathological experiments to investigate the *in vivo* anti-inflammatory and healing effects of RNP. As depicted in Fig. 7a and Fig. S34, histological examination of the healed wound was performed using hematoxylin-eosin (H&E) and Masson's trichrome (MT) staining. Notably, due to the small diameter of the punching needle, no extensive damage to the artery wall was observed, and the inflammatory response was confined to the puncture site. To ensure accurate assessment of the puncture areas, aortas from the PCL and RNP groups are sliced to a thickness of 40 μm. All sections are stained with H&E, and the regions exhibiting the most pronounced inflammatory response were selected for subsequent analysis. As shown in the H&E staining, the control group exhibits minimal inflammatory infiltrates, whereas the PCL group displays distinct areas of inflammatory cell infiltration (indicated by larger blue nuclei), and the RNP group shows smaller affected areas. Meanwhile, MT staining reveals greater collagen deposition in the RNP group compared to the PCL group, approaching levels observed in the control. This indicates that RNP accelerates injury healing by reducing inflammation and promoting collagen deposition.

Next, we assess the role of RNP in alleviating oxidative stress and inflammation at the injury site. Tumor necrosis factor-α (TNF-α) immunohistochemical staining and macrophage density analysis via CD68 immunofluorescence (IF) staining have been performed (Fig. 7b and c). Notably, the number of macrophages in the RNP group is significantly lower than in the PCL group, with statistical significance, and is consistent with the Sham group (Fig. 7f and g). Furthermore, IF staining for iNOS (a pro-inflammatory marker) and IL-10 (an anti-inflammatory marker) revealed a significant down-regulation of iNOS and an up-regulation of IL-10 in the RNP-treated group in comparison to the PCL-treated group, and the expression patterns of RNP are similar in the Sham group (Fig. 7d–h, i). These findings indicate that RNP effectively reduces inflammation at the injury site. Additionally, angiogenesis, a key indicator of graft healing, was evaluated by IF staining for α-SMA, VEGF, and CD31. Both markers exhibit notably higher expression in the RNP group compared to the PCL group (Fig. 7e–j). These results demonstrate that RNP exhibits superior pro-vascularization properties and enhances wound healing more effectively than PCL. Consequently, graft healing in arteries can be accelerated by reducing inflammation, promoting collagen deposition, and fostering neoangiogenesis.

Last but not least, the biosafety of the RNP biotube *in vivo* has been evaluated on day 7 post-operation through H&E histological staining of key organs (heart, liver, spleen, lung, and kidney) and serum biochemistry analysis (Figs. S35 and 36). These results distinctly indicate that no significant damage or abnormalities are observed in the major body organs and tissues, suggesting its minimal cytotoxicity. To assess the long-term safety of RNP, hematological indices, including WBC, lymphocyte, and granulocyte counts, have been measured on day 20 post-operation. As shown in Fig. S37, there is a negligible difference between the RNP-treated rats and the controls. Taken together, our experiments demonstrate that RNP serves as an effective and safe antioxidant-mimetic biotube, combating oxidative stress and promoting rapid graft healing through the reduction of inflammation, collagen deposition, neoangiogenesis, and the prevention of surgical adhesion in rats.

4. Conclusion

In this study, we have developed a novel antioxidase-mimetic biotube (RNP) incorporating Ru nanocluster-anchored NiMOF onto a PCL scaffold designed to combat oxidative stress and inflammation in vascular repair. Our experimental studies have shown that the unique Ni–O–Ru interface in RNP biotube regulates the electronic structure of the Ru active site through rapid charge transfer, thereby endowing the biotube with versatile antioxidase-like properties. Remarkably, RNP biotube exhibits highly efficient SOD-like activity (91 % ROS elimination rate) and high CAT-like activity (84 % H_2O_2 conversion rate). Therefore, RNP can protect the survival and proliferation of HUVEC cells in high-ROS-level milieus by preventing oxidative stress-mediated cell apoptosis, thereby enhancing their angiogenic potential. As a result, the RNP biotube facilitates superior artery healing, reducing inflammation and promoting neovascularization in a rat injury model. Furthermore, RNP with good biocompatibility shows low cytotoxicity in rats, with no signs of organ damage or abnormal hematological indices. These results highlight the great potential of RNP as an innovative vascular graft, offering a promising strategy for developing ROS-scavenging and anti-inflammatory biotubes for vascular repair and the treatment of various oxidative stress-related diseases.

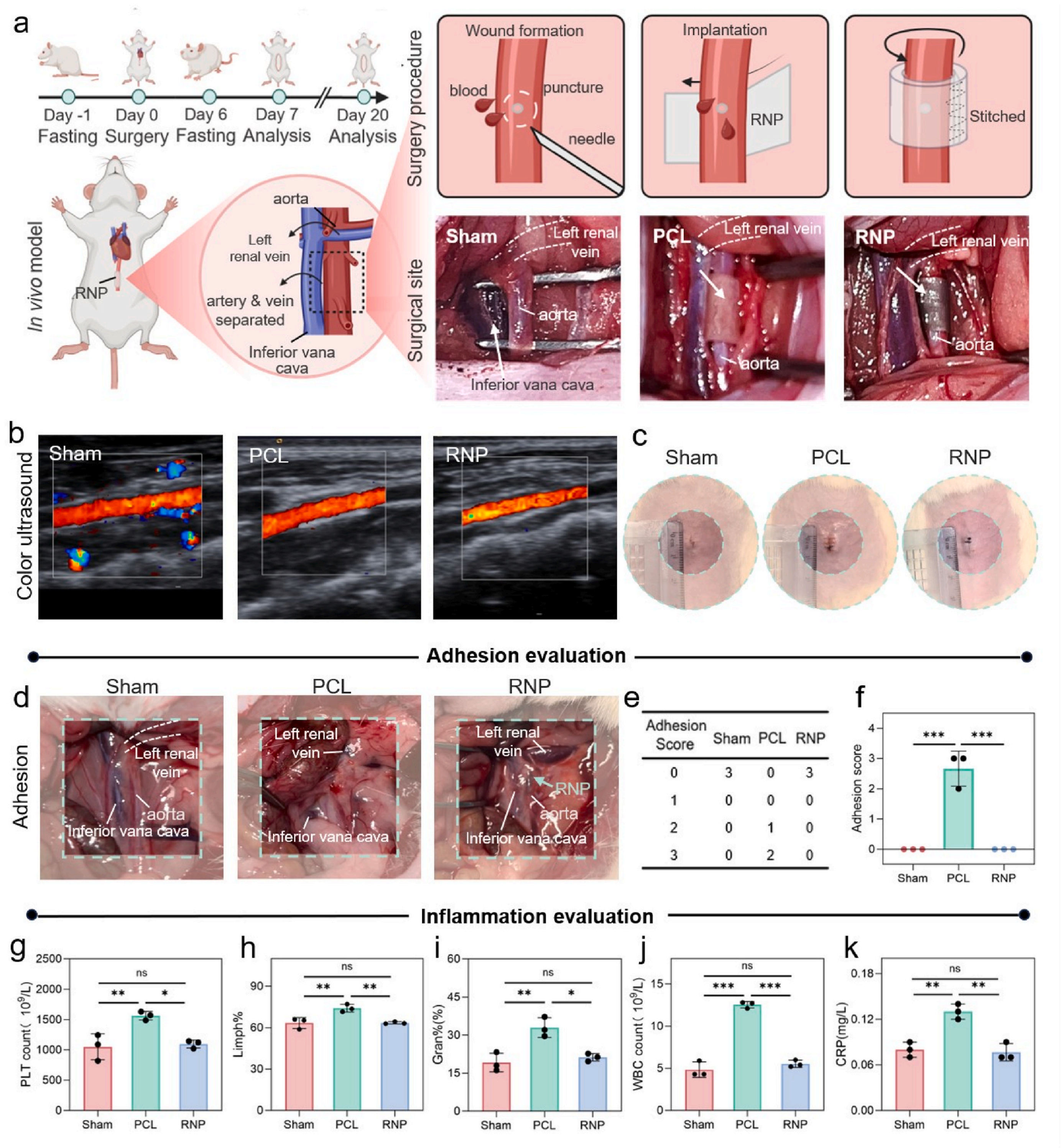

Adhesion Score	Sham	PCL	RNP
0	3	0	3
1	0	0	0
2	0	1	0
3	0	2	0

Fig. 6. Artificial biotube alleviates inflammation. (a) *In vivo* demonstration of RNP implantation in the rat model. (b) The Doppler ultrasound images of the rat abdomen for the Sham, PCL, and RNP groups on the 7th day after surgery. (c) Cutaneous surgical wound healing condition on postoperative day 7. (d) Representative photographs depicting the adhesions in each group on postoperative day 7. (e, f) Quantitative scoring analysis of different samples on postoperative day 7. Assessment of (g) cell count of PLT, (h) percentage of Limph, (i) percentage of Gran, and (j) cell count of WBC. (k) Assessment of CRP via serum biochemical study. Data are presented as mean ± SD from independent replicates (n ≥ 3). n. s., non-significant were assessed by one-way ANOVA.

CRediT authorship contribution statement

Guliyaer Aini: Writing – review & editing, Writing – original draft, Investigation, Formal analysis, Data curation, Conceptualization. **Jianmei Ren:** Investigation, Formal analysis. **Haojie Xu:** Methodology, Formal analysis, Data curation. **Yang Gao:** Methodology. **Tiantian Li:** Methodology, Formal analysis. **Lang Ma:** Supervision, Project administration, Data curation. **Li Qiu:** Supervision, Methodology. **Evgeniya Sheremet:** Writing – review & editing, Supervision. **Shuang Li:** Supervision, Formal analysis. **Chong Cheng:** Writing – review & editing,

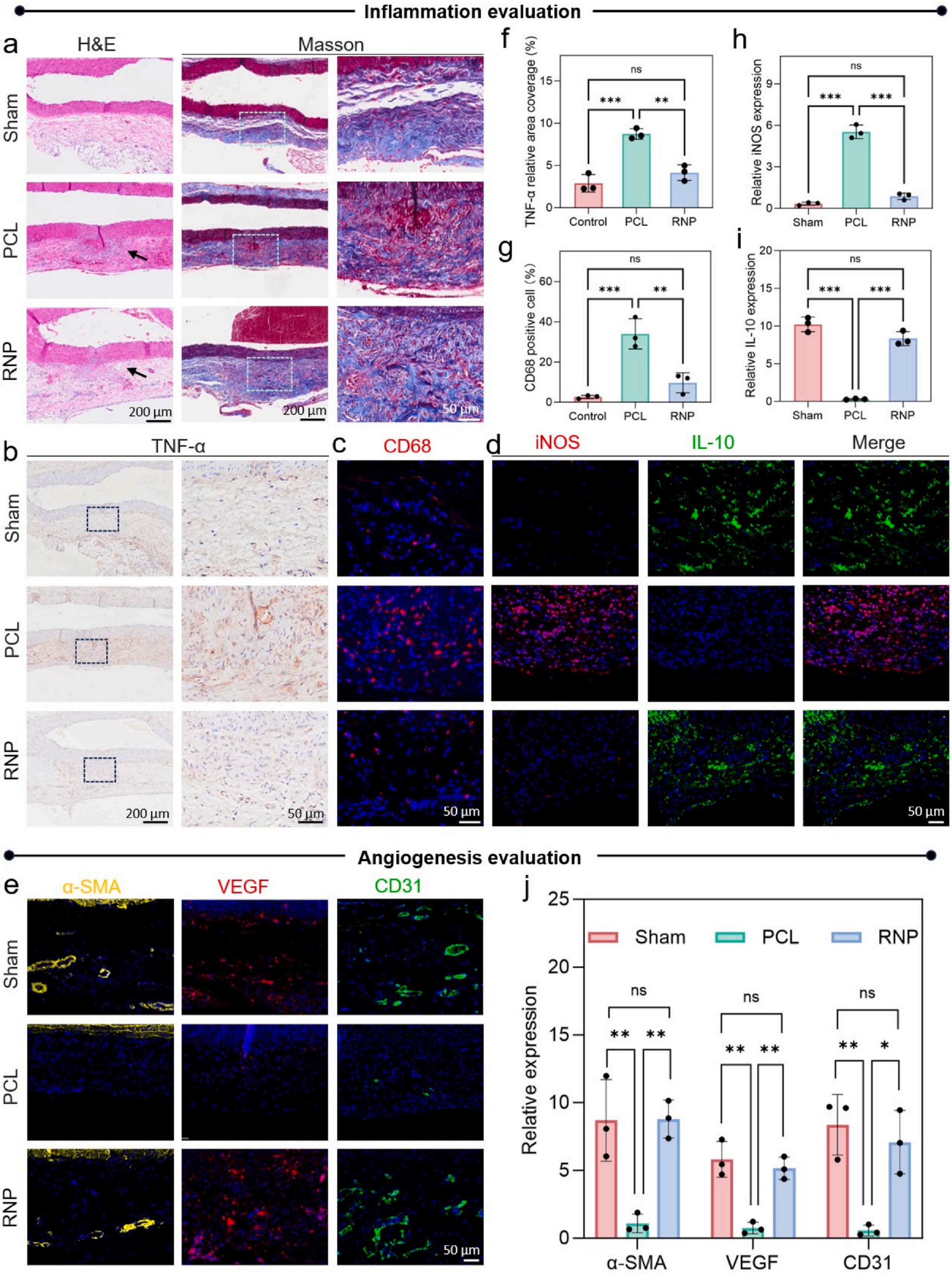

Fig. 7. ***In vivo* anti-inflammatory and pro-angiogenesis effects of RNP.** (a) H&E and Masson staining of the punching site for the aortas of different groups on day 7. (b) The aortas of each group are visualized using IHC staining with TNF-α antibody. (c) CD68/DAPI, (d) iNOS/DAPI and IL-10/DAPI, and (e) α-SMA/DAPI, VEGF/DAPI, and CD31/DAPI fluorescence images of the aortic wall histological sections in all groups. (f–j) Quantitative statistics of TNF-α, CD68, iNOS, IL-10, α-SMA, VEGF, and CD31 respectively. Data are presented as mean ± SD from independent replicates ($n \geq 3$). n. s., non-significant were assessed by one-way ANOVA.

Supervision, Conceptualization. **Tian Ma:** Writing – review & editing, Project administration, Conceptualization. **Changsheng Zhao:** Writing – review & editing, Supervision, Conceptualization.

Declaration of competing interest

We declare that we have no financial and personal relationships with other people or organizations that can inappropriately influence our work, there is no professional or other personal interest of any nature or kind in any product, service and/or company that could be construed as influencing the position presented in, or the review of, the manuscript entitled.

Acknowledgments

This work was financially supported by the National Natural Science Foundation of China (Nos. 52473136 and 52203177) and the Science and Technology Project of Sichuan Province (2025YFHZ0188). Dr. Ma acknowledges the financial support of the State Key Laboratory of Polymer Materials Engineering (Grant No. sklpme2025-2-10). The authors would like to thank and express their heartfelt gratitude to Huifang Li, Yan Wang, and Fei Chen (all from Core Facilities, West China Hospital, Sichuan University) for their assistance with the flow cytometry measurements and pathological analysis. We want to express our gratitude for the drawing materials provided by BioRender. The Sichuan University Animal Ethics Committee approved all the experimental protocols; the assigned approval number is 20230818003. The procedure for collecting blood from human volunteers has been approved by the Institute of Blood Transfusion, Chinese Academy of Medical Sciences' Institutional Review Board (IRB, Ethics approval number: No. 2024553).

Appendix A. Supplementary data

Supplementary data to this article can be found online at https://doi.org/10.1016/j.biomaterials.2025.123790.

Data availability

Data will be made available on request.

References

[1] A.J. Weiss, M.L. Ros, A. Correa, N. Barman, J.E. Tamis-Holland, Curr Atheroscler, Rep 24 (2022) 731.
[2] E. Abyzova, E. Dogadina, R.D. Rodriguez, I. Petrov, Y. Kolesnikova, M. Zhou, C. Liu, E. Sheremet, Mater. Today Bio 22 (2023) 100784.
[3] B. Ratner, BME Front. 4 (2023) 3.
[4] B. Zhang, R. Yao, C. Hu, M.F. Maitz, H. Wu, K. Liu, L. Yang, R. Luo, Y. Wang, Biomaterials 269 (2021) 120418.
[5] J. Lin, X. Chen, Y. Li, L. Yu, Y. Chen, B. Zhang, Mater. Today Bio 26 (2024) 101037.
[6] J. Nan, C. Xia, J. Zhang, Y. Xie, S. Shi, W. Yang, M. Yu, Y. Chen, J. Zhang, Biomaterials 322 (2025) 123379.
[7] Y. Wang, H. Wu, Z. Zhou, M.F. Maitz, K. Liu, B. Zhang, L. Yang, R. Luo, Y. Wang, Sci. Adv. 8 (2022) eabm3378.
[8] J. Li, J. Zhang, P. Yu, H. Xu, M. Wang, Z. Chen, B. Yu, J. Gao, Q. Jin, F. Jia, J. Ji, G. Fu, Bioact. Mater. 37 (2024) 239.
[9] B. Yang, C. Hu, Y. Zhang, D. Jiang, P. Lin, S. Qiu, J. Shi, L. Wang, J. Am. Chem. Soc. 146 (2024) 17201.
[10] Z. Chen, J. Duan, Y. Diao, Y. Chen, X. Liang, H. Li, Y. Miao, Q. Gao, L. Gui, X. Wang, J. Yang, Y. Li, Bioact. Mater. 6 (2021) 1.
[11] J. Kong, R. Zou, R. Chu, N. Hu, J. Liu, Y. Sun, X. Ge, M. Mao, H. Yu, Y. Wang, ACS Nano 18 (2024) 4140.
[12] P. Patil, K. A. Russo, J. T. McCune, A. C. Pollins, M. A. Cottam, B. R. Dollinger, C. R. DeJulius, M. K. Gupta, R. D'Arcy, J. M. Colazo, F. Yu, M. G. Bezold, J. R. Martin, N. L. Cardwell, J. M. Davidson, C. M. Thompson, A. Barbul, A. H. Hasty, S. A. Guelcher, C. L. Duvall,Sci. Transl. Med., 14, eabm6586.
[13] Z. Yang, H. Shi, G. Cai, S. Jiang, Z. Hu, Z. Wang, Small 19 (2023) 2302284.
[14] L. Cheng, Z. Zhuang, M. Yin, Y. Lu, S. Liu, M. Zhan, L. Zhao, Z. He, F. Meng, S. Tian, L. Luo, Nat. Commun. 15 (2024) 9786.
[15] C. Geng, S. He, S. Yu, H.M. Johnson, H. Shi, Y. Chen, Y.K. Chan, W. He, M. Qin, X. Li, Y. Deng, Adv. Mater. 36 (2024) 2310599.
[16] L. Li, Z. Cao, C. Zhang, L. Li, Q. Li, C. Liu, C. Qu, R. Luo, P. Fu, Y. Wang, Adv. Funct. Mater. 34 (2024) 2312243.
[17] M. Sun, H. Li, Y. Hou, N. Huang, X. Xia, H. Zhu, Q. Xu, Y. Lin, L. Xu, Sci. Adv. 9 (2023) eade6973.
[18] B. Huang, S. Li, S. Dai, X. Lu, P. Wang, X. Li, Z. Zhao, Q. Wang, N. Li, J. Wen, Y. Liu, X. Wang, Z. Man, W. Li, B. Liu, Adv. Sci. 11 (2024) 2400229.
[19] Z. Song, H. Yu, L. Hou, Y. Dong, M. Hu, P. Wei, W. Wang, D. Qian, S. Cao, Z. Zheng, Z. Xu, B. Zhao, Y. Huang, W. Jing, X. Zhang, Adv. Funct. Mater. 34 (2024) 2315382.
[20] C.S. Shin, F.J. Cabrera, R. Lee, J. Kim, R. Ammassam Veettil, M. Zaheer, A. Adumbumkulath, K. Mhatre, P.M. Ajayan, S.A. Curley, B.G. Scott, G. Acharya, Adv. Mater. 33 (2021) 2003778.
[21] Z. Li, L. Li, M. Yue, Q. Peng, X. Pu, Y. Zhou, Adv. Mater. 36 (2024) 2402738.
[22] Y. Liu, T. Chao, Y. Li, P. Peng, G. Ge, D. Geng, L. Dong, C. Wang, Nat. Commun. 16 (2025) 3629.
[23] H. He, X. Wei, B. Yang, H. Liu, M. Sun, Y. Li, A. Yan, C.Y. Tang, Y. Lin, L. Xu, Nat. Commun. 13 (2022) 4242.
[24] Y. Shen, S. Li, X. Hou, J. Yu, Y. Zhu, C. Zhao, Z. Niu, X. Guan, B. Xiong, S. Wang, Y. Yang, X. Li, L. Sun, S. Wu, B. Huang, H. Xu, H. Yin, Adv. Sci. (2025) 2500720.
[25] S. Ghosh, M. Zheng, J. He, Y. Wu, Y. Zhang, W. Wang, J. Shen, K.W.K. Yeung, P. Neelakantan, C. Xu, W. Qiao, Biomaterials 314 (2025) 122908.
[26] J. He, J. Niu, L. Wang, W. Zhang, X. He, X. Zhang, W. Hu, Y. Tang, H. Yang, J. Sun, W. Cui, Q. Shi, Biomaterials 306 (2024) 122475.
[27] D.K. Zhi, Q.H. Cheng, A.C. Midgley, Q.Y. Zhang, T.T. Wei, Y. Li, T. Wang, T.Z. Ma, M. Rafique, S. Xia, Y.J. Cao, Y.C. Li, J. Li, Y.Z. Che, M.F. Zhu, K. Wang, D.L. Kong, Sci. Adv. 8 (2022) eabl3888.
[28] L. Yang, W. Li, X. Ding, Y. Zhao, X. Qian, L. Shang, Adv. Funct. Mater. 35 (2025) 2410927.
[29] X. Xue, H. Zhang, H. Liu, S. Wang, J. Li, Q. Zhou, X. Chen, X. Ren, Y. Jing, Y. Deng, Z. Geng, X. Wang, J. Su, Adv. Funct. Mater. 32 (2022) 2202470.
[30] B. Zavan, C. Gardin, V. Guarino, T. Rocca, I. Cruz Maya, F. Zanotti, L. Ferroni, G. Brunello, J.C. Chachques, L. Ambrosio, V. Gasbarro, Nanomaterials 11 (2021) 751.
[31] J. Wang, J. Lin, L. Chen, L. Deng, W. Cui, Adv. Mater. 34 (2022) 2108325.
[32] W. Lee, C. Xu, H. Fu, M. Ploch, S. D'Souza, S. Lustig, X. Long, Y. Hong, G. Dai, Adv. Funct. Mater. 34 (2024) 2313942.
[33] J. Fu, N. Zhang, C. Xu, M. Zhao, S. Wu, S. Xu, X. Hong, M. Wang, G. Fu, ACS Nano 19 (2025) 451.
[34] H. Liu, Y. Liu, H. Wang, Q. Zhao, T. Zhang, S.A. Xie, Y. Liu, Y. Tang, Q. Peng, W. Pang, W. Yao, J. Zhou, Adv sci 9 (2022) e2203995.
[35] J.L. Liu, T. Wang, C.C. Liao, W. Geng, J. Yang, S.X. Ma, W.D. Tian, L. Liao, C. Cheng, Adv. Mater. 36 (2024) 2411618.
[36] J. Guo, Z. Xing, L. Liu, Y. Sun, H. Zhou, M. Bai, X. Liu, M. Adeli, C. Cheng, X. Han, Adv. Funct. Mater. 33 (2023) 2211778.
[37] K.S. Washington, C.A. Bashur, Front. Pharmacol. 8 (2017) 659.
[38] A. Joorabloo, T. Liu, Explorations 4 (2024) 20230066.
[39] B. Yang, H. Yao, J. Yang, C. Chen, J. Shi, Nat. Commun. 13 (2022) 1988.
[40] S. Zhang, Y. Li, S. Sun, L. Liu, X. Mu, S. Liu, M. Jiao, X. Chen, K. Chen, H. Ma, T. Li, X. Liu, H. Wang, J. Zhang, J. Yang, X.-D. Zhang, Nat. Commun. 13 (2022) 4744.
[41] D. Yang, M. Yuan, J. Huang, X. Xiang, H. Pang, Q. Wei, X. Luo, C. Cheng, L. Qiu, L. Ma, ACS Nano 18 (2024) 3424.
[42] B. Xu, Y. Huang, D. Yu, Y. Chen, Biomaterials 316 (2025) 123026.
[43] H. Ma, X. Zhang, L. Liu, Y. Huang, S. Sun, K. Chen, Q. Xin, P. Liu, Y. Yan, Y. Wang, Y. Li, H. Liu, R. Zhao, K. Tan, X. Chen, X. Yuan, Y. Li, Y. Liu, H. Dai, C. Liu, H. Wang, X.-D. Zhang, Sci. Adv. 9 (2023) eadh7828.
[44] X. Liu, S. Chen, Y. Yan, L. Liu, Y. Chen, Biomaterials 286 (2022) 121594.
[45] X. Liu, S. Chen, J. Huang, Y. Du, Z. Luo, Y. Zhang, L. Liu, Y. Chen, Nat. Nanotechnol. 19 (2024) 1745.
[46] M. Liang, Q. Wang, S. Zhang, Q. Lan, R. Wang, E. Tan, L. Zhou, C. Wang, H. Wang, Y. Cheng, Adv. Mater. 36 (2024) 2409015.
[47] Y. Li, X. Li, T. Chen, J. Li, J. Qi, W. Li, Nat. Commun. 16 (2025) 6445.
[48] H. An, X. Qiu, X. Wang, C. Du, X. Guo, S. Hou, M. Xu, J. Wang, C. Cheng, H. Ran, P. Li, Z. Wang, Z. Zhou, J. Ren, W. Jiang, Biomaterials 315 (2025) 122972.
[49] M. Long, L. Wang, L. Kang, D. Liu, T. Long, H. Ding, Y. Duan, H. He, B. Xu, N. Gu, ACS Nano 19 (2025) 4561.
[50] L. Li, Q. Wen, T. Wang, S. Xiao, Y. Gao, M. Wang, X. Xu, L. Ma, C. Cheng, Mater. Today 78 (2024) 142.
[51] L. Wang, B. Zhu, Y. Deng, T. Li, Q. Tian, Z. Yuan, L. Ma, C. Cheng, Q. Guo, L. Qiu, Adv. Funct. Mater. 31 (2021) 2101804.
[52] J. Liu, Z. Chen, H. Liu, S. Qin, M. Li, L. Shi, C. Zhou, T. Liao, C. Li, Q. Lv, M. Liu, M. Zou, Y. Deng, Z. Wang, L. Wang, Small 20 (2024) 2305076.
[53] F. Chen, Q. Tang, T. Ma, B. Zhu, L. Wang, C. He, X. Luo, S. Cao, L. Ma, C. Cheng, InfoMat 4 (2022) e12299.
[54] Y. Wei, Y. Zhou, H. Yuan, Y. Liu, Y.-W. Lin, J. Su, X. Tan, Int. J. Mol. Sci. 23 (2022) 2652.
[55] W. Zhang, X. Dai, X. Jin, M. Huang, J. Shan, X. Chen, H. Qian, Z. Chen, X. Wang, Smart Mater. Med. 4 (2023) 134.
[56] Y.M. Sun, S.D. Mu, Z.Y. Xing, J.S. Guo, Z.H. Wu, F.Y. Yu, M.R. Bai, X.L. Han, C. Cheng, L. Ye, Adv. Mater. 34 (2022) 2206208.
[57] Y. Zhang, W. Zheng, H. Wu, R. Zhu, Y. Wang, M. Wang, T. Ma, C. Cheng, Z. Zeng, S. Li, SusMat 4 (2024) 106.
[58] J. Liu, L. Shi, Y. Wang, M. Li, C. Zhou, L. Zhang, C. Yao, Y. Yuan, D. Fu, Y. Deng, M. Liu, G. Wang, L. Wang, Z. Wang, Nano Today 47 (2022) 101627.
[59] M. Bai, T. Wang, Z. Xing, H. Huang, X. Wu, M. Adeli, M. Wang, X. Han, L. Ye, C. Cheng, Nat. Commun. 15 (2024) 9592.

[60] A. Carton, A. Mesbah, T. Mazet, F. Porcher, M. Francois, Solid State Sci. 9 (2007) 465.

[61] S. Yuan, J. Peng, B. Cai, Z. Huang, A.T. Garcia-Esparza, D. Sokaras, Y. Zhang, L. Giordano, K. Akkiraju, Y.G. Zhu, R. Huebner, X. Zou, Y. Roman-Leshkov, Y. Shao-Horn, Nat. Mater. 21 (2022) 673.

[62] T. Wang, C. Wang, X. Yang, R. Ma, Q. Yang, W. Shi, Z. Xia, H. Ma, Q. Wei, S. Chen, Chem. Eng. J. 475 (2023) 146273.

[63] J. Li, F. Luo, Q. Zhao, Z. Li, H. Yuan, D. Xiao, J. Mater. Chem. A 2 (2014) 4690.

[64] Y. Sun, Z. Xue, Q. Liu, Y. Jia, Y. Li, K. Liu, Y. Lin, M. Liu, G. Li, C.-Y. Su, Nat. Commun. 12 (2021) 1369.

[65] D. Chen, R.H. Yu, R.H. Lu, Z.H. Pu, P.Y. Wang, J.W. Zhu, P.X. Ji, D.L. Wu, J.S. Wu, Y. Zhao, Z.K. Kou, J. Yu, S.C. Mu, InfoMat 4 (2022) e12287.

[66] Z. Wu, J. Shen, C. Li, C. Zhang, K. Feng, Z. Wang, X. Wang, D.M. Meira, M. Cai, D. Zhang, S. Wang, M. Chu, J. Chen, Y. Xi, L. Zhang, T.-K. Sham, A. Genest, G. Rupprechter, X. Zhang, L. He, ACS Nano 17 (2023) 1550.

[67] Q. Liu, B. Lu, F. Nichols, J. Ko, R. Mercado, F. Bridges, S. Chen, SusMat 2 (2022) 335.

[68] X. Gu, M. Yu, S. Chen, X. Mu, Z. Xu, W. Shao, J. Zhu, C. Chen, S. Liu, S. Mu, Nano Energy 102 (2022) 107656.

[69] G. Li, H. Jang, S. Liu, Z. Li, M.G. Kim, Q. Qin, X. Liu, J. Cho, Nat. Commun. 13 (2022) 1270.

[70] J. Yang, Y. Shen, Y. Sun, J. Xian, Y. Long, G. Li, Angew. Chem. Int. Ed. 62 (2023) e202302220.

[71] Z. Wu, J. Yang, W. Shao, M. Cheng, X. Luo, M. Zhou, S. Li, T. Ma, C. Cheng, C. Zhao, Adv. Fiber Mater. 4 (2022) 774.

[72] K. Rui, G. Zhao, M. Lao, P. Cui, X. Zheng, X. Zheng, J. Zhu, W. Huang, S.X. Dou, W. Sun, Nano Lett. 19 (2019) 8447.

[73] M. Du, S. Liu, N. Lan, R. Liang, S. Liang, M. Lan, D. Feng, L. Zheng, Q. Wei, K. Ma, Regen. Biomater. 11 (2024) rbad114.

[74] L. Qi, Y. Huang, Z. Liu, J. Liu, J. Wang, H. Xu, H. Yang, L. Liu, G. Feng, S. Zhang, Y. Li, L. Zhang, Adv. Fiber Mater. 6 (2024) 1777.

[75] Y. Chen, X. Dong, M. Shafiq, G. Myles, N. Radacsi, X. Mo, Adv. Fiber Mater. 4 (2022) 959.

[76] Y. Xie, S. Xiao, L. Huang, J. Guo, M. Bai, Y. Gao, H. Zhou, L. Qiu, C. Cheng, X. Han, ACS Nano 17 (2023) 15097.

[77] H. Yan, Y. Peng, Y. Huang, M. Shen, X. Wei, W. Zou, Q. Tong, N. Zhou, J. Xu, Y. Zhang, Y.-X. Ye, G. Ouyang, Adv. Mater. 36 (2024) 2311535.

[78] X. Zhang, Y. Wan, Y. Wen, Y. Zhu, H. Liu, J. Qiu, Z. Zhu, Z. Sun, X. Gao, S. Bai, Y. Zhang, L. Zhang, X. Yan, J. Zhang, Y. Liu, S. Li, L.-D. Zhao, Nat. Catal. 8 (2025) 465.

[79] N. Wen, Y. Huang, Y. Yang, H. Wang, D. Wang, H. Chen, Q. Peng, X.Y. Kong, L. Ye, ACS Catal. 14 (2024) 11153.

[80] T. Wang, M. Bai, W. Geng, M. Adeli, L. Ye, C. Cheng, Nat. Commun. 16 (2025) 856.

[81] G. Pan, X. Hou, Z. Liu, C. Yang, J. Long, G. Huang, J. Bi, Y. Yu, L. Li, ACS Catal. 12 (2022) 14911.

[82] C. Hui, Y. Gao, B.-Y. Yan, L.-Q. Ding, T.-C. Sun, Z. Liu, S. Ramakrishna, Y.-Z. Long, J. Zhang, Chem. Eng. J. 464 (2023) 142458.

[83] Y. Shen, C. Tang, B. Sun, Y. Wu, X. Yu, J. Cui, M. Zhang, M. El-Newehy, H. El-Hamshary, P. Barlis, W. Wang, X. Mo, Adv. Healthcare Mater. 13 (2024) 2304293.

[84] Y. Deng, Y. Gao, T. Li, S. Xiao, M. Adeli, R.D. Rodriguez, W. Geng, Q. Chen, C. Cheng, C. Zhao, ACS Nano 17 (2023) 2943.

[85] C.H. Liu, Y. Cao, Y.R. Cheng, D.D. Wang, T.L. Xu, L. Su, X.J. Zhang, H.F. Dong, Nat. Commun. 11 (2020).

[86] L. Wen, H. Qiu, S. Li, Y. Huang, Q. Tu, N. Lyu, X. Mou, X. Luo, J. Zhou, Y. Chen, C. Wang, N. Huang, J. Xu, Acta Biomater. 179 (2024) 371.

[87] H. Ji, K. Yu, S. Abbina, L. Xu, T. Xu, S. Cheng, S. Vappala, S.M.A. Arefi, M.M. Rana, I. Chafeeva, M. Drayton, K. Gonzalez, Y. Liu, D. Grecov, E.M. Conway, W. Zhao, C. Zhao, J.N. Kizhakkedathu, Nat. Mater. 24 (2025) 626.

[88] J. Qi, X. Li, Y. Cao, Y. Long, J. Lai, Y. Yao, Y. Meng, Y. Wang, X.-D. Chen, H. Vankelecom, X. Bian, W. Cui, Y. Sun, Biomaterials 309 (2024) 122615.

[89] Y. Kang, L. Xu, J. Dong, X. Yuan, J. Ye, Y. Fan, B. Liu, J. Xie, X. Ji, Nat. Commun. 15 (2024) 1042.

[90] J. Tu, J. Min, Y. Song, C. Xu, J. Li, J. Moore, J. Hanson, E. Hu, T. Parimon, T.-Y. Wang, E. Davoodi, T.-F. Chou, P. Chen, J.J. Hsu, H.B. Rossiter, W. Gao, Nat. Biomed. Eng. 7 (2023) 1293.